

DUST IN THE IONIZED MEDIUM OF THE GALAXY: GHRS MEASUREMENTS OF Al III AND S III¹

J. CHRISTOPHER HOWK AND BLAIR D. SAVAGE

Department of Astronomy, University of Wisconsin–Madison, Madison, WI 53706; howk, savage@astro.wisc.edu

Received 1998 June 16; accepted 1999 January 10

ABSTRACT

We present interstellar absorption-line measurements of the ions S III and Al III toward the stars β^1 Sco, μ Col, ξ Per, ζ Oph, ρ Leo, and HD 18100 using archival data from the Goddard High-Resolution Spectrograph on board the *Hubble Space Telescope*. The ions Al III and S III trace heavily depleted and nondepleted elements, respectively, in ionized gas along the sight lines to these late-O/early-B stars. We use the photoionization equilibrium code CLOUDY to derive the ionization correction relating the ratio $N(\text{Al III}) / N(\text{S III})$ to the gas-phase abundance $[\text{Al/S}]_i$ [$\equiv \log(N(\text{Al})/N(\text{S}))_i - \log(\text{Al/S})_\odot$] in the ionized gas. For spectral types considered here, the corrections range from 0.1 to 0.3 dex and are independent of the assumed ionization parameter, i.e., the ratio of ionizing photon density to mean electron density. Using the results of these photoionization models, we find $[\text{Al/S}]_i \sim -1.0$ in the ionized gas toward β^1 Sco, ξ Per, and ζ Oph; along the low-density path toward μ Col we find $[\text{Al/S}]_i \approx -0.8$. Since S is not depleted onto grains, these values of $[\text{Al/S}]_i$ ($\approx [\text{Al/H}]_i$) imply that Al-bearing grains are present in the ionized nebulae around these stars. If the warm ionized medium (WIM) of the Galaxy is photoionized by OB stars, the observations of ρ Leo and HD 18100 imply $[\text{Al/S}]_i = -0.4$ to -0.5 in the WIM and thus the presence of dust grains containing Al in this important phase of the interstellar medium. While photoionization appears to be the most likely origin of the ionization for Al III and S III, we cannot rule out confusion from the presence of hot, collisionally ionized gas along the sight lines to β^1 Sco and HD 18100. We find that $[\text{Al/S}]_i$ in the ionized gas along the six sight lines is anticorrelated with the electron density and average sight-line neutral density. The degree of grain destruction in the ionized medium of the Galaxy is not much higher than in the warm neutral medium. The existence of grains in the ionized regions studied here has important implications for the thermal balance of these regions.

Subject headings: dust, extinction — Galaxy: halo — H II regions — ISM: abundances — ultraviolet: ISM

1. INTRODUCTION

Warm (10^4 K) ionized hydrogen is an important component of our Galaxy's interstellar medium (ISM). The diffuse warm ionized medium (WIM) of the Galaxy has a mass surface density one-third that of neutral hydrogen (H I), with an extended vertical scale height ($h_z \approx 900$ pc) and a power requirement equivalent to the total kinetic energy injected into the ISM by supernovae (Kulkarni & Heiles 1987; Reynolds 1991b). The WIM has principally been studied through the detection of faint emission lines (e.g., Reynolds et al. 1998b) and through the dispersion measures of radio emission from distant pulsars (Taylor & Cordes 1993; Reynolds 1991a).

The goal of this work is to determine if there is evidence for dust grains in the ionized medium of the Galaxy, including low-density H II regions and the diffuse WIM. The distinction between H II regions and the WIM in this work is mainly one of distance from the source of ionization and possibly fractional ionization. The existence of dust in the WIM of the Galaxy has important ramifications for the heating (and cooling) of the gas and possibly also for the power requirements of the ionization. Photoelectric emission of electrons from the surfaces of dust grains is an important source of heating in the warm neutral medium (WNM) of the Galaxy (Wolfire et al. 1995a). Reynolds &

Cox (1992) have shown that, if grains are present in the WIM, photoelectric emission may be the dominant source of heating in the WIM and may also be responsible for the enhanced forbidden-line strengths that are characteristic of the WIM (e.g., Dettmar & Shulz 1992; Rand 1997, 1998).

To provide evidence for the existence of dust in this important phase of the ISM, we will measure the gas-phase abundance of Al relative to S in ionized gas. In the WNM, relative gas-phase abundances, derived from absorption-line spectroscopy, have been used to infer the elemental composition of dust grains (see Savage & Sembach 1996b and references therein). We apply this method to the ionized medium of the Galaxy.

Absorption-line spectroscopy of interstellar material yields column densities of species independent of the prevailing physical conditions (e.g., T_e and n_e). In Table 1 we list the properties of several possibly important probes of weakly ionized gas in the vacuum ultraviolet. Along with the wavelengths and f -values (from Morton 1991) for the transitions given, we also give relevant ionization potentials, logarithmic solar-system abundances of the elemental species relative to H (Anders & Grevesse 1989; Grevesse & Noels 1993), and representative values of the gas-phase abundances of each of the elemental species in warm neutral halo gas (see Savage & Sembach 1996b). The lines and ionic species listed in Table 1 are those likely to provide measurable column densities in the spectral range accessible to the UV spectrographs previously or currently on *Hubble Space Telescope* (HST; ~ 1120 – 3200 Å) and lines accessible to the *Far-Ultraviolet Spectroscopic Explorer*, which will cover

¹ Based on observations made with the NASA/ESA *Hubble Space Telescope*, obtained from the data archive at the Space Telescope Science Institute, which is operated by the Association of Universities for Research in Astronomy, Inc., under the NASA contract NAS 5-26555.

TABLE 1
UV PROBES OF WEAKLY IONIZED GAS

Ion (1)	λ^a (Å) (2)	f^b (3)	IP		$\log \{X/H\}_\odot^c$ (+12.00) (6)	$[X/H]_{\text{halo}}^d$ (7)	$\log N(X)_{\text{H II}}^e$ (cm ⁻²) (8)	τ_0^f (9)
			(X ⁱ⁻¹ → X ⁱ) (eV) (4)	(X ⁱ → X ⁱ⁺¹) (eV) (5)				
C III.....	977.020	0.762	24.4	47.9	8.55	-0.4 ^g	14.46	86.4
N II.....	1083.990	0.103	14.5	29.6	7.97	0.0	14.88	36.9
N III.....	989.799	0.107	29.6	47.4	7.97	0.0	14.11	5.95
Si III.....	1206.500	1.67	16.3	33.5	7.55	-0.25	13.96	111.7
Fe III.....	1122.526	0.0788	16.2	30.7	7.51	-0.6	13.78	4.6
S III.....	1190.208	0.0222	23.3	34.8	7.27	0.0	14.02	1.81
	1012.502	0.0355	23.3	34.8	7.27	0.0	14.02	2.46
Ar II.....	919.781	0.00887	15.8	27.6	6.56	0.0 ^h	13.37	0.14
Al III.....	1862.789	0.279	18.8	28.4	6.48	-0.6 ⁱ	12.42	0.82
	1854.716	0.560	18.8	28.4	6.48	-0.6 ⁱ	12.42	1.65
Cr III.....	1040.050	0.122	16.5	31.0	5.68	-0.35	12.21	0.17
	1033.331	0.0640	16.5	31.0	5.68	-0.35	12.21	0.09
	1030.100	0.0625	16.5	31.0	5.68	-0.35	12.21	0.09
P III.....	1334.813	0.0253	19.7	30.2	5.57	0.0	12.30	0.04
	998.000	0.112	19.7	30.2	5.57	0.0	12.30	0.14
Ti III.....	1298.697	0.0951	13.6	27.5	4.93	-0.65	11.28	0.02
	1295.884	0.0668	13.6	27.5	4.93	-0.65	11.28	0.01

^a Vacuum wavelengths from Morton (1991).

^b Oscillator strengths from Morton (1991).

^c The logarithmic “solar” abundances of the elements, $\log \{X/H\}_\odot$. We have adopted the solar system meteoritic abundances from Anders & Grevesse (1989) except for C, which is the photospheric value from Grevesse & Noels (1993).

^d Typical values of the logarithmic normalized gas-phase abundance seen in warm neutral halo clouds, defined in such a way that $[X/H] = \log (N(X)/N(\text{H})) - \log \{X/H\}_\odot$. These values are for the warm cloud at $v_\odot \approx +41$ km s⁻¹ seen toward μ Col (Sofia, Savage, & Cardelli 1993; Shull & York 1977), which is typical of “halo”-type neutral clouds (Howk et al. 1998).

^e Expected column density of each species for a fully ionized cloud with $\log N(\text{H II}) = 19.0$ cm⁻² as calculated using the CLOUDY photoionization equilibrium code (see § 4.1). The assumed gas-phase abundances of each of the elements are dictated by the solar system values modified by the normalized gas-phase abundances typical of halo material. The shape of the ionizing spectrum was taken to be that of an O9.5V star with $T_{\text{eff}} = 33,000$ K.

^f Expected peak optical depth of each line assuming the column densities given in col. (8) with b -values appropriate for gas at $T = 10,000$ K and no nonthermal broadening.

^g The gas-phase abundance of C has only been measured accurately in cool neutral clouds found in the disk. We tentatively adopt the Cardelli et al. (1993) average $[C/H] \approx -0.4$ for our “halo” abundances.

^h The ratio Ar I/H I has recently been measured to be significantly subsolar along a number of low- $N(\text{H I})$, partially ionized sight lines by Sofia & Jenkins (1998). However, these authors argue that the large ionization cross-section of Ar⁰ implies that much of the Ar may reside in the form of Ar⁺, which they did not observe. We therefore adopt $[\text{Ar}/\text{H}] \approx 0.0$ in warm neutral halo gas.

ⁱ The abundance of Al is poorly known in the WNM, because the Al II $\lambda 1670$ line requires very large saturation corrections (Barker et al. 1984). We have assumed $[\text{Al}/\text{H}] \approx [\text{Fe}/\text{H}]$.

the wavelength range $\sim 905\text{--}1195$ Å after its launch in early 1999. The last two columns of Table 1 give the expected column density of each ionic tracer for a completely ionized region with halo-like abundances having $\log N(\text{H II}) = 19.0$ (where $N(\text{H II})$ is expressed in cm⁻²) and total hydrogen density $n_{\text{H}} = 1.0$ cm⁻³, as well as the expected peak optical depth of each line in the case of pure thermal broadening with $T = 10^4$ K. These optical depths will be less if non-thermal broadening plays a significant role (a likely situation).

Those ions from Table 1 accessible to *HST* include S III, Al III, P III, Si III, and Ti III. Given the great strength or weakness of many of the lines from Table 1, one is typically able to measure a tracer of a nondepleted element (see Spitzer & Fitzpatrick 1993, hereafter SF93; Fitzpatrick & Spitzer 1994, 1997) in the ionized gas (S III)² and a tracer of a refractory element in ionized gas (Al III) in the *HST* bandpass. Relatively little is known about the Galactic dis-

tribution of these ionized gas tracers. Savage, Edgar, & Diplax (1990) used the *International Ultraviolet Explorer* to study the distribution of Al III in the Galaxy. They find an exponential scale-height of $h_{\text{Al III}} = 1.02_{-0.24}^{+0.36}$ kpc for the distribution of Al III, thereby showing the distribution of Al III is slightly more extended than the neutral gas ($h_{\text{H I}} = 0.67_{-0.16}^{+0.21}$ kpc toward these same objects) and similar to that of free electrons. From the ratios of the estimated vertical column densities of Al III and free electrons (which are assumed to trace the protons of the WIM), they infer a gas-phase abundance of $[\text{Al}/\text{H}]_i > -1.7$ in the ionized gas (using the solar system abundance Al/H given in Table 1). Sembach & Savage (1992) have also studied the properties of Al III absorption toward a number of halo stars. They find that the absorption due to Al III is significantly different than that of the more highly ionized species Si IV, C IV, and N V.

In this work we present observations of interstellar absorption due to the ions S III and Al III along the sight lines to six late-O/early-B stars: ξ Per (HD 24912), ζ Oph (HD 149757), β^1 Sco (HD 144217), μ Col (HD 38666), ρ Leo (HD 91316), and HD 18100. These spectra are taken from the Goddard High-Resolution Spectrograph (GHRS) data

² In many sight lines the S III $\lambda 1190.208$ line is blended with intermediate-velocity absorption from the strong Si II line at 1190.416 Å ($v \approx +52$ km s⁻¹ relative to S III); this is particularly true for observations made at intermediate-resolution (FWHM $\gtrsim 15$ km s⁻¹).

archive. The stellar and sight-line properties relevant to this study are given in Table 2. The first four targets are relatively nearby disk stars ($z \lesssim 200$ pc). For these sight lines, the column density of ionized gas is likely dominated by H II region material, i.e., by fully ionized gas immediately surrounding these stars. For the latter two stars, which are more distant and at high latitude, the paths through the ionized ISM are dominated by the WIM, by which we mean diffuse gas at large distances from any ionizing star. The species Al III and S III require more energy for creation than the H⁺ typically used to probe the WIM; however, these ions likely represent significant fractions of the S and Al associated with the WIM. In all cases we depend upon the use of an ionization correction factor to determine the relative abundances presented here. However, we will show that these small corrections are relatively insensitive to model assumptions.

In § 2 we discuss the GHRs archival data and our reductions and analysis of these data. This includes in § 2.2 a description of the component-fitting analysis required for two of our six sight lines and measurements of Fe III from the literature in § 2.3. We discuss the physical conditions and velocity structure of the ionized gas in § 3; we include in this a description of the complex kinematics along the sight line to ζ Oph in § 3.1.1. We use the photoionization code CLOUDY (Ferland 1996; Ferland et al. 1998) to model ionized regions about hot stars in § 4 and use the results of these models to derive the gas-phase Al/S abundance in the ionized gas of the Galaxy. The abundances imply the existence of dust in the ionized gas toward these six stars. We also discuss in § 4.4 the confusing effects of collisionally ionized gas along our six sight lines. In § 5 we discuss the implications of our derived abundances and dust in the ionized phase of the Galaxy. A summary of our work and major conclusions is given in § 6.

2. GHRs ARCHIVAL DATA

In this section we discuss our reduction of the GHRs archival data and measurements of interstellar absorption

features in these data. A more complete discussion can be found in Howk, Savage, & Fabian (1999). Included in this section (§ 2.2) is a description of our approach to model component-fitting. Component-fitting is required to disentangle the S III $\lambda 1190.208$ absorption line from the strong Si II line at 1190.416 \AA in intermediate-resolution data. Also, we discuss the literature values of Fe III $\lambda 1122.526$ absorption used in this paper (§ 2.3).

2.1. Reductions and Measurements

We have retrieved the GHRs archival data containing the S III and Al III transitions for the stars listed in Table 2. The STScI archive identification codes and relevant information, including exposure times, grating mode, and aperture, are given for each spectrum in Table 3. The spectra have been calibrated using the standard CALHRS routine, which includes conversion of raw counts to count rates and corrections for particle radiation contamination, dark counts, known diode nonuniformities, paired pulse events, and scattered light. The final data reduction was performed using software developed and tested at the University of Wisconsin–Madison. This includes the merging of individual spectra and allowing for additional refinements to the scattered light correction for the echelle-mode data (Cardelli, Ebbets, & Savage 1993).

The spectra used for this study include data taken both before and after the installation of the Corrective Optics Space Telescope Axial Replacement (COSTAR). For information regarding the pre-COSTAR performance of the GHRs, see Heap et al. (1995); the post-COSTAR performance of the GHRs is discussed by Robinson et al. (1998). The pre-COSTAR data used here were taken through the Small Science Aperture (SSA), thereby avoiding the complication of the very broad wings found in the pre-COSTAR Large Science Aperture (LSA) line-spread function (LSF). The GHRs echelle-mode spectra (Ech-A and Ech-B) used here have a resolution of $\sim 3.5 \text{ km s}^{-1}$ (FWHM). The observations of the S III $\lambda 1190$ region using the G160M grating have a velocity resolution of $\sim 20 \text{ km s}^{-1}$, but in the Al III $\lambda\lambda 1855, 1862$ region the resolution is

TABLE 2
STELLAR AND SIGHT-LINE PROPERTIES

Star [HD (Name)]	l (deg)	b (deg)	d^a (pc)	z^b (pc)	Spectral Type	T_{eff}^c (K)	$E(B-V)^d$ (mag)	$\langle n(\text{H}) \rangle^e$ (cm^{-3})	$\langle n_e \rangle^f$ (cm^{-3})
24912 (ζ Per)	160.4	−13.1	540	122	O7.5 I	36,000	0.33	1.2	1.4
38666 (μ Col)	237.3	−27.1	400	180	O9.5 V	33,000	0.01	0.06	0.2
149757 (ζ Oph)	6.3	+23.6	140	56	O9.5 V	31,900	0.32	3.1	4.0
144217 (β^1 Sco)	353.2	+23.6	160	60	B0.5 V	28,000	0.20	2.9	...
91316 (ρ Leo)	234.9	+52.8	870	690	B1 Ib	26,800	0.05	0.10	0.07
18100	217.9	−62.7	3100	2800	B1 V	26,400	0.02	0.01	0.07

^a Distances, with the exception of ρ Leo and HD 18100, are based upon *Hipparcos* measurements of stellar parallax (Perryman et al. 1997). The distance estimates to ρ Leo and HD 18100 are from Keenan, Brown, & Lennon (1986) and Diplas & Savage (1994), respectively.

^b Distance from the midplane of the Galaxy given the derived distances.

^c Adopted effective temperatures for each of the stars. These data are from the following: Code et al. (1976, ζ Oph); Holmgren et al. (1997, β^1 Sco); Howarth & Prinja (1989, μ Col); Keenan et al. (1986, HD 18100); Keenan & Dufton (1983, ρ Leo); Sokolov (1995, 23 Ori); and Vacca, Garmany, & Shull (1996; ζ Per).

^d The dust color excess, $E(B-V)$, is taken from Diplas & Savage (1994).

^e Average line of sight neutral hydrogen densities toward these stars, where $\langle n(\text{H}) \rangle \equiv \{N(\text{H I}) + 2N(\text{H}_2)\}/d$. We have taken values for $N(\text{H I})$ from Diplas & Savage (1994) and $N(\text{H}_2)$ from Bohlin, Savage, & Drake (1978). The value listed for HD 18100 is $\langle n(\text{H I}) \rangle$.

^f Electron densities along these lines of sight, when available. The data presented here are from Howk et al. (1999, μ Col); Reynolds (1988, ζ Per and ζ Oph); Savage & Sembach (1996b, HD 18100); and this work (ρ Leo). The values quoted for ζ Per and ζ Oph are the values $\langle n^2 \rangle^{1/2}$ characteristic of the H II regions surrounding these stars. For μ Col the value quoted is $\langle n_e \rangle$ of the H II region. The values quoted for HD 18100 and ρ Leo are the values $\langle n_e \rangle$ of the warm ionized gas in these directions.

TABLE 3
LOG OF GHRS ARCHIVAL DATA

Star	Spectral Range (Å)	Root Name ^a	Exposure ^b (s)	Mode and Order ^c	Aperture ^d	FP-SPLIT/COSTAR? ^e
ζ Per (HD 24912)	1187.7–1194.2	Z0GY010LT	691.2	Ech-A/47	SSA	4/F
	1857.1–1867.4	Z0GY011ST	172.8	Ech-B/30	SSA	4/F
μ Col (HD 38666)	1184.8–1191.1	Z2AF010PT	108.8	Ech-A/47	LSA	0/T
	1184.8–1191.1	Z2C0020PP	108.8	Ech-A/47	LSA	0/T
	1846.7–1856.9	Z2D40118T	54.4	Ech-B/30	LSA	0/T
	1859.8–1869.8	Z2CX010LT	27.2	Ech-B/30	LSA	0/T
	1855.9–1866.0	Z2D4020KT	54.4	Ech-B/30	LSA	0/T
ζ Oph (HD 149757)	1188.6–1195.0	Z2VX010CT	691.2	Ech-A/47	SSA	4*/T
	1189.8–1196.2	Z2VX010ET	691.2	Ech-A/47	SSA	4*/T
	1856.9–1866.9	Z0LD020TT	172.8	Ech-B/30	SSA	4*/F
β ¹ Sco (HD 144217)	1180.1–1216.3	Z0YU010AT	172.8	G160M/01	SSA	4/F
	1856.7–1866.7	Z0YU020AT	172.8	Ech-B/30	SSA	4*/F
ρ Leo (HD 91316)	1188.7–1195.3	Z2ZX010CT	870.4	Ech-A/47	SSA	4/T
	1852.7–1862.9	Z0ZI0314T	86.4	Ech-B/30	SSA	0/F
	1853.5–1863.6	Z0ZI0315T	86.4	Ech-B/30	SSA	0/F
	1854.3–1864.4	Z0ZI0316T	86.4	Ech-B/30	SSA	0/F
	1855.0–1865.1	Z0ZI0317T	86.4	Ech-B/30	SSA	0/F
HD 18100	1181.4–1217.6	Z13Z010AT	1324.8	G160M/01	SSA	4/F
	1842.9–1876.9	Z13Z010NM	1209.6	G160M/01	SSA	4/F

^a STScI archival root name.

^b Total exposure time given in s.

^c Grating mode and spectral order used for the observation.

^d Aperture used for the observation. The LSA subtends 1'74 × 1'74 on the sky for post-COSTAR observations, 2'0 × 2'0 for pre-COSTAR data. The pre-COSTAR SSA subtends 0'25 × 0'25, and the post-COSTAR SSA is 0'22 × 0'22 on the sky.

^e The number of FP-SPLIT subexposures composing each observation. Asterisks mark those observations for which we have explicitly derived the fixed-pattern noise spectrum and removed it. This column also notes with a "T" those observations taken after the installation of COSTAR, and with an "F" for those taken before COSTAR.

~11 km s⁻¹ (FWHM). For the G160M data we have used the SPYBAL observations taken before the science integrations to refine the absolute velocity scales (see Soderblom, Sherbert, & Hulbert 1993, 1994). The SPYBAL observations contain emission lines observed in the wavelength range ~1500–1540 Å range. We have calculated the average offset between the observed and expected wavelengths of these lines and applied these wavelength offsets to the appropriate science observations (Soderblom et al. 1994). Using the SPYBAL observations, we find offsets of -0.003 and -0.033 Å, respectively, are appropriate for the S III and Al III observations toward HD 18100. Toward β¹ Sco the G160M observations of S III require an offset of -0.014 Å. These wavelength adjustments should make the absolute velocities for the G160M observations good to ~3 km s⁻¹. The velocity scale of the echelle data presented here is likely good to ±1 resolution element (i.e., 3.5 km s⁻¹).

Much of the data presented here employed the FP-SPLIT=4 procedure, which takes four exposures at different grating carousel positions. These scans are identified in Table 3. The FP-SPLIT exposures can be used to solve for the fixed-pattern noise spectrum of the GHRS (Cardelli & Ebbets 1994) and remove it from the observations. In general, we have solved for the fixed-pattern noise but only applied the solution in the cases where the noise spectrum showed significant structure within a few hundred km s⁻¹ of the line of interest. In this way we avoid adding noise to those spectra with few or no fixed-pattern features. Only for the ζ Oph scans and the echelle observations of Al III toward β¹ Sco was there structure deemed to be possibly significant to the current work; these are the only observations for which we have applied the fixed-pattern noise solutions.

We have normalized the spectra using low-order (≤4) Legendre polynomial fits to the local stellar continuum in regions free from interstellar absorption. Figures 1 and 2 present the normalized absorption-line profiles of S III and Al III for the stars considered here. Also shown in Figure 1 are the profiles of Zn II λλ2026.14 or 2062.66. The Zn II profiles trace the column density of neutral material along these sight lines. Absorption from the Si II λ1190 line can be seen in all of the plots showing the S III absorption. The expected shift of the Si II line relative to S III is +52.4 km s⁻¹. If intermediate negative velocity Si II is present, it can be blended with the S III line. The S III + Si II profile toward the star ρ Leo is a good example of this behavior: narrow intermediate velocity Si II features are present at v_⊙ ≈ +12 and +25 km s⁻¹ relative to the rest frame S III along this sight line. These two features make it impossible to determine the S III absorption for v_⊙ > 5 km s⁻¹. Therefore our study of the ρ Leo sight line is limited to v_⊙ < 5 km s⁻¹. The behavior of Si II can be determined from the Si II λ1193.29 transition.

Table 4 contains the measured equivalent widths and column densities of interstellar S III and Al III toward our six targets, along with the 1 σ uncertainties in these quantities. These uncertainties include contributions from photon statistics, continuum placement uncertainties, and zero-level uncertainties. We have adopted a 2% zero-level uncertainty throughout. This may overestimate the errors in regions near heavily saturated lines, i.e., in the wavelength region of S III. See Sembach & Savage (1992; their Appendix) and Howk et al. (1999) for a more thorough discussion of these sources of uncertainty.

For the echelle data the values of the column densities presented in Table 4 were derived by a straight integration

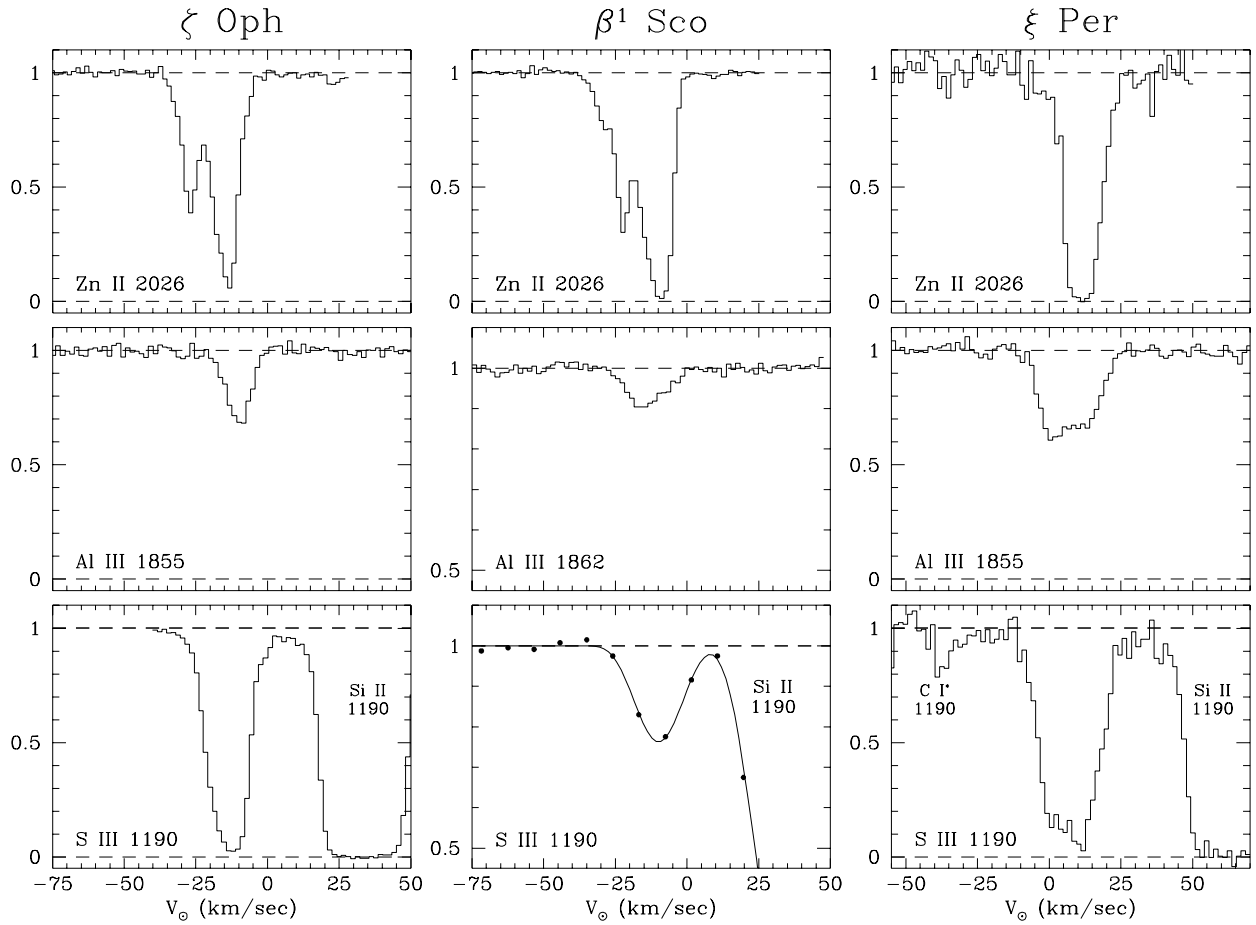


FIG. 1.—Continuum-normalized absorption-line profiles of Zn II, Al III, and S III for the disk stars ζ Per, ζ Oph, and β^1 Sco are displayed on a heliocentric velocity scale. Echelle-mode data are plotted as histograms. The G160M data for the S III profile toward β^1 Sco are plotted as points, and the component model convolved with the instrumental spread function is overplotted as the solid line (see § 2.2). Strong Si II λ 1190.416 absorption is seen in the S III λ 1190.208 region of the spectrum ($v = +52.4$ km s $^{-1}$ relative to S III).

TABLE 4
EQUIVALENT WIDTHS AND COLUMN DENSITIES OF S III, Al III, AND Fe III

Star	$W_\lambda \pm \sigma$ (mÅ) ^a			$\log N \pm \sigma$ (cm $^{-2}$) ^b		
	S III (λ 1190.2)	Al III (λ 1854.7)	Al III (λ 1862.8)	S III	Al III	Fe III ^c
ζ Per	87 ± 3	...	51.2 ± 1.7	14.82 ± 0.02	12.85 ± 0.02	...
μ Col	16.3 ± 0.6	15.0 ± 2.0	9.9 ± 1.5	13.82 ± 0.02	12.01 ± 0.05	$13.37^{+0.09}_{-0.11}$
ζ Oph	66.6 ± 1.4	...	19.7 ± 0.8	14.76 ± 0.02	12.42 ± 0.02	13.45 ± 0.10
β^1 Sco	27 ± 5^d	...	9.5 ± 0.7	13.98 ± 0.08^d	12.06 ± 0.04	13.10 ± 0.10
ρ Leo	12.7 ± 0.8^e	17.5 ± 1.6^e	...	13.72 ± 0.03^e	12.06 ± 0.04^e	...
HD 18100.....	54 ± 8^d	74 ± 6	40 ± 6	14.29 ± 0.06^d	12.70 ± 0.04	...

^a Equivalent widths W_λ in mÅ for the lines of S III and Al III with 1σ uncertainties.

^b Column densities of interstellar S III and Al III in units of atoms cm $^{-2}$. Also given are the 1σ error estimates for these measurements.

^c The Fe III column densities quoted here are taken from the following: Howk et al. (1999, μ Col); Morton (1975, ζ Oph); and Savage & Bohlin (1979, β^1 Sco). These column densities are all derived from the Fe III λ 1122.5 line. The latter two are based upon *Copernicus* observations, and the former comes from GHRs G160M observations. The *Copernicus* observations have been adjusted by -0.15 dex to account for newer oscillator strengths (Morton 1991; $f = 0.07884$) and the errors are estimates by the current authors. In the case of ζ Oph and possibly β^1 Sco, C I absorption could be contributing to these column densities. For μ Col Howk et al. (1999) have put restrictive limits on the degree of this contamination and find it not to be significant compared with the quoted uncertainties.

^d These values are based upon GHRs G160M data and have been derived through a component-fitting analysis.

^e These values are for the velocity range $-19 \leq v_\odot \leq +2$ km s $^{-1}$, which corresponds to the uncontaminated velocity range for the S III absorption. The total integrated sight-line values for Al III are $W_\lambda = 29 \pm 3$ mÅ and $\log N(\text{Al III}) = 12.27 \pm 0.05$.

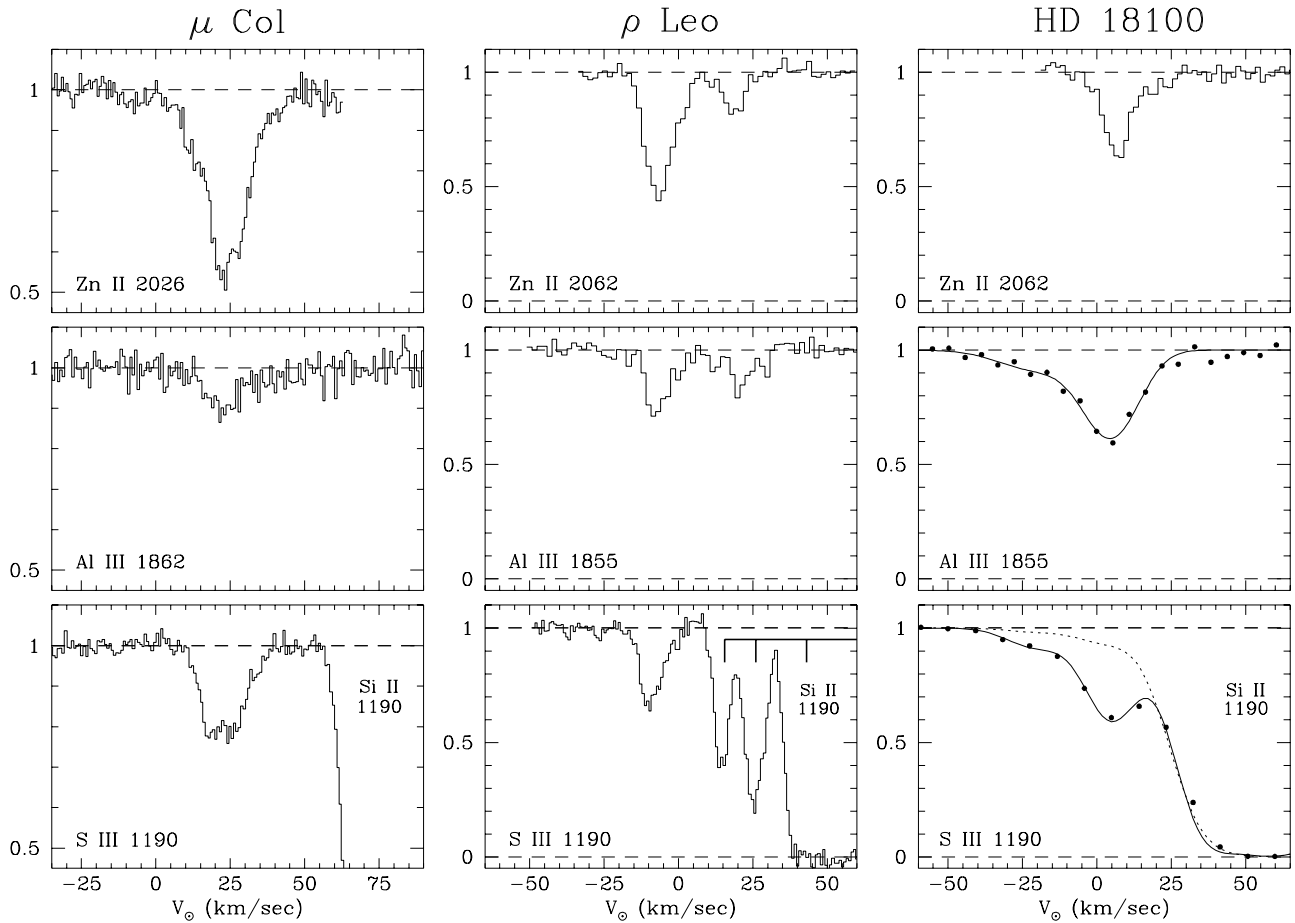


FIG. 2.—Same as for Figure 1 but for the higher z stars μ Col, ρ Leo, and HD 18100. The G160M data for the Al III and S III profiles toward HD 18100 are overplotted with the component model convolved with the instrumental LSF; the dashed line in the S III profile for this star shows the absorption model for Si II λ 1190 derived from the Si II λ 1193 transition (see § 2.2).

of the apparent column density profiles (Savage & Sembach 1991). In the absence of unresolved saturated structure, $N_a(X^i) = N(X^i)$, where $N_a(X^i)$ and $N(X^i)$ are the apparent and true column densities of the ion X^i , respectively. The S III lines observed toward ζ Per and ζ Oph are the only profiles for which we might expect the presence of unresolved saturated structure. Although the profiles seem resolved by the echelle-mode resolution, the value $N(\text{S III})$ for the ζ Per and ζ Oph sight lines may underestimate the total column density. For gas at $T = 10^4$ K, the thermal Doppler spread parameters for S III and Al III are $b(\text{S III}) \approx 2.3 \text{ km s}^{-1}$ and $b(\text{Al III}) \approx 2.5 \text{ km s}^{-1}$ (FWHM ~ 3.8 and 4.2 km s^{-1} , respectively). Thus the profiles of photoionized gas traced by these species should be marginally resolved, even without the likely addition of nonthermal broadening.

As mentioned above, intermediate-velocity Si II absorption is seen toward ρ Leo at velocities near the rest frame of S III. In both the Al III and Zn II profiles, an absorbing component is present near $v_\odot \approx +20 \text{ km s}^{-1}$. The corresponding S III absorption is blended with the intermediate-velocity Si II absorption. Therefore we report the column densities of Al III and S III for this sight line integrated over the velocity range $v_\odot = -19$ to $+2 \text{ km s}^{-1}$. This only includes the lower velocity Al III absorbing component. We do not expect any Si II absorption in this velocity range given the profile of the Si II λ 1193.29 line present in the same GHRS observation.

2.2. Component-Fitting Measurements

The S III λ 1190.208 lines observed toward β^1 Sco and HD 18100 with the G160M grating are blended with the nearby Si II λ 1190.416 line ($v = +52.4 \text{ km s}^{-1}$ relative to S III). To assess the extent of the blending, we have performed a component-fitting analysis of these profiles using software kindly provided to us by E. Fitzpatrick and described in SF93. A model of the interstellar absorption was convolved with the instrumental LSF appropriate for the pre-COSTAR SSA, and the value of χ^2 minimized between this model and the data. The LSF adopted here for the SSA follows Spitzer & Fitzpatrick (1995) in using instrumental LSF given for the G160M grating in the GHRS Instrument Handbook (v3.0; Duncan 1992, that paper's Table 4–8). The LSF is well characterized by a Gaussian with a FWHM ≈ 1.08 diodes at the detector array. From these models, we derive the best-fit column density, N_k , Doppler parameter, b_k , and central velocity, $\langle v \rangle_k$, for the k -absorbing components of Si II and S III along these lines of sight.

For the β^1 Sco observations, we have used the high-resolution GHRS Ech-B observations of the Si II λ 1808.013 line along this sight line to provide more information about the component structure of the Si II λ 1190 line. We have fitted the λ 1808 line with a four-component model and subsequently fixed the values of N_k and b_k from this fit, although allowing common shifts in the velocities, to

describe the Si II $\lambda 1190$ absorption. The S III column density presented for β^1 Sco in Table 4 is derived from the best-fit one component model. Figure 1 displays the G160M data for this sight line as points, and the model derived from our fitting is displayed as a solid line. The central velocity for the S III profile is $\langle v_{\odot} \rangle = -10.0 \pm 0.4 \text{ km s}^{-1}$ (fitting error only). The b -value is not well constrained but is likely significantly less than the resolution of the G160M observations.

For the sight line toward HD 18100, no high-resolution observations of Si II were available. However, we have fitted the Si II $\lambda 1193.290$ line present in the G160M observation to assess the contribution of intermediate-velocity Si II absorption to the S III profile. The model fit to the Si II $\lambda 1193$ profile is overplotted as the dotted line on the S III profile for HD 18100 in Figure 2. This model has been scaled by the appropriate factor to account for the differing oscillator strengths of the 1190 and 1193 transitions of Si II and shifted to the velocity scale of S III. It is clear from this presentation that there is a component of Si II overlapping the S III absorption in velocity. We have held the column density of this Si II component fixed when fitting the S III + Si II blend at 1190 Å. We find the Si II component is relatively weak, of order 12% of the S III column density at these velocities. Table 4 gives the total column density derived for S III along this sight line. The total column density of S III we obtain agrees with the value $\log N(\text{S III}) = 14.26 \pm 0.06$ derived by Savage & Sembach (1996a, hereafter SS96).

We have similarly fitted the Al III profile for HD 18100 with a component model. We find evidence for at least two components in the S III and Al III absorption along this sight line. While the b -values are ill-constrained and likely much less than the G160M instrumental resolution, the column densities and central velocities for the individual absorbing components of S III are as follows:

$$\langle v_{\odot} \rangle_1 = -20 \pm 6 \text{ km s}^{-1},$$

$$\log N(\text{S III})_1 = 13.51 \pm 0.25, \quad (1)$$

$$\langle v_{\odot} \rangle_2 = +5.8 \pm 0.9 \text{ km s}^{-1},$$

$$\log N(\text{S III})_2 = 14.21 \pm 0.03. \quad (2)$$

For Al III we find:

$$\langle v_{\odot} \rangle_1 = -19 \pm 13 \text{ km s}^{-1},$$

$$\log N(\text{Al III})_1 = 12.1 \pm 0.4, \quad (3)$$

$$\langle v_{\odot} \rangle_2 = +4.8 \pm 1.6 \text{ km s}^{-1},$$

$$\log N(\text{Al III})_2 = 12.58 \pm 0.11 \quad (4)$$

We do not believe unresolved saturation is a significant problem for either species for this sight line. Column densities derived for the two Al III transitions through a straight integration of the are the $N_a(v)$ profiles are the same within the errors, and their $N_a(v)$ profiles show no evidence for saturation effects (see Savage & Sembach 1994; their Figure 4). For the S III profile we find that the equivalent width is within the range covered by the two Al III transitions, and the peak optical depth is very similar to that found in the Al III $\lambda 1855$ profile (though it includes a small contribution from the overlapping Si II $\lambda 1190$ line). The data for Al III and S III along the sight line to HD 18100 are shown in Figure 2 as points, and the component models for each species are plotted as solid lines. Considering the difficulty in deriving precise values for the $\langle v_{\odot} \rangle_1 \sim -20 \text{ km s}^{-1}$ component, we

will use the integrated sight-line column densities in our analysis. We also note that the component structure buried in the intermediate-resolution G160M data may be significantly more complex than our component-fitting analysis suggests (see SS96; Ryans, Sembach, & Keenan 1996).

2.3. Literature Measurements of Fe III

For the stars μ Col, β^1 Sco, and ζ Oph, measurements of the Fe III $\lambda 1122.526$ line are available. Howk et al. (1999) report on the profile and column density of Fe III toward μ Col as measured with the GHRM using the G140M grating. Savage & Bohlin (1979) and Morton (1975) report on the gas-phase column density of Fe III toward β^1 Sco and ζ Oph, respectively, based upon *Copernicus* measurements. The column densities derived by these authors for Fe III are given in Table 4. The data derived from the earlier *Copernicus* papers have been modified to reflect more recent determinations of the f -values of this transition (Morton 1991). We adopt $f = 0.0788$, which amounts to a modification of -0.15 dex to the column densities adopted in the works of Savage & Bohlin (1979) and Morton (1975).

The Fe III absorption toward β^1 Sco and ζ Oph could be substantially blended with C I absorption at $\lambda\lambda 1122.438$ and 1122.518 . Howk et al. (1999) have put restrictive limits on the degree of contamination to the Fe III absorption toward μ Col. They find the level of contamination is not significant compared with the errors. For the *Copernicus* results, we have estimated the errors quoted in Table 4, although these column densities should be considered upper limits due to the possible contamination from C I absorption.

3. PHYSICAL CONDITIONS AND VELOCITY STRUCTURE OF THE IONIZED GAS

The sight lines to the stars in our sample cover a wide range of physical conditions and environments. The absorption lines due to ionized gas along the sight lines toward β^1 Sco, ζ Oph, and ξ Per are likely dominated by photoionized gas in the H II regions of these disk stars. The sight lines toward the higher latitude stars sample the WIM of the Galaxy. Toward μ Col, the gas being sampled may well be a mixture of both H II region and WIM gas, although to our knowledge no H II region has previously been identified about this star. Given the range of conditions and velocity structure, we mention some of the more important aspects of these ionized gas properties here.

3.1. H II Region Sight Lines

The H II regions of some of our disk stars have been studied in detail. Reynolds & Ogden (1982) and Reynolds (1988) have studied the H II region S27 surrounding ζ Oph. Their analysis of faint H α and [S II] emission from the nebula suggests $\langle n_e^2 \rangle^{1/2} = n_e f^{1/2} \approx 4 \text{ cm}^{-3}$ with $T_e \approx 6700$ K, where n_e is the local electron density and f is the volume-filling factor. Reynolds (1988) has similarly studied Sivan 4, the H II region surrounding ξ Per. The H α and [S II] emission suggest $\langle n_e^2 \rangle^{1/2} = n_e f^{1/2} \approx 1.4 \text{ cm}^{-3}$ for this nebula with $T_e \approx 8000$ K. Howk et al. (1999) and Shull & York (1977) have derived $\langle n_e \rangle = 0.2 \text{ cm}^{-3}$ for the ionized gas along the line of sight toward μ Col, which is similar to that in the Galactic WIM. This average density has been derived from analyses of the excited states of Si II and N II, respectively, and is a lower limit to the true electron density.

The H α emission toward ξ Per is centered at $v_{\odot} = +7 \text{ km s}^{-1}$ (Reynolds 1988). Emission from the nebula S220 1°

to the north, which is also thought to be powered by ζ Per, is centered at $v_{\odot} = +12 \text{ km s}^{-1}$. These velocities are well within the limits of Al III and S III absorption toward this star. Toward ζ Oph the H α emission is centered at $v_{\odot} = -13 \text{ km s}^{-1}$ (Reynolds 1988), which is roughly consistent with the Al III absorption and the positive-velocity edge of the S III absorption.

Recent observations with the Wisconsin H α Mapper (WHAM) Fabry-Perot instrument (M. Haffner 1998, private communication) have similarly shown that H α -emitting gas toward μ Col lies at velocities quite similar to the center of S III and Al III absorption along this sight line. The sight line toward this star may be associated with an H II region, the WIM along this sight line, or a combination of both. At the distance and latitude of μ Col, we expect only $\sim 20\%$ of the WIM in the direction of μ Col to be in front of the star (Reynolds 1991b). Given that the H α emission in this direction is at velocities consistent with the S III profile presented here, even though the WIM along this direction should mostly come from beyond the star, we will assume the emission and absorption along the sight line toward μ Col are mostly probing H II region gas.

When comparing the velocities of the tracers of ionized gas being studied here and tracers of neutral gas, such as Zn II, we see three distinct arrangements in the nearby disk stars. The ionized gas along the sight line to β^1 Sco is found at velocities between those of the major components observed in the low-ionization species. The Al III and S III absorption toward μ Col resides at velocities similar to the principal component seen in neutral gas tracers. For both of the stars ζ Oph and ξ Per, we find a component of low-ionization absorption that is aligned with one edge of the S III profile. The low-ionization components found at this edge are significantly narrower than the S III absorption profile. There is no systematic trend when comparing the velocity structure of neutral and ionized gas tracers along these low- z sight lines.

3.1.1. The Complicated Case of ζ Oph

The velocity structure observed in tracers of ionized gas along the path to ζ Oph is quite complex and warrants a more complete description. The profiles of Al III, S III, and Zn II toward ζ Oph shown in Figure 1 have distinctly different velocity structure. The S III absorption is broader than either the Zn II or Al III profiles and is asymmetric. The Zn II absorption lines up well with the negative velocity edge of the S III profile, and the Al III absorption is aligned quite well with the positive velocity edge.

Sembach, Savage, & Jenkins (1994) studied the Al III, Si IV, and C IV absorption along this sight line in some detail. These authors attributed the Al III and Si IV absorption to the photoionized nebula about ζ Oph and suggested the velocity offsets seen between these two species indicated the H II region was expanding. In Figure 3 we plot the apparent column density profiles (see Savage & Sembach 1991) of the ions Al III, Si IV, and S III. The Si IV and Al III profiles have been scaled upward by factors of 40 and 100, respectively. The lower panel of Figure 3 shows the log of the apparent column density ratios of Al III and Si IV to S III as a function of velocity. The value of $\log(N(\text{Al III})/N(\text{S III}))$ varies by about 1 dex between the peak of the Al III profile at $v_{\odot} \approx -8 \text{ km s}^{-1}$ and the peak Si IV absorption near $v_{\odot} \approx -15 \text{ km s}^{-1}$. The component at $v_{\odot} \approx -15 \text{ km s}^{-1}$ coincides in velocity with the dense neutral/molecular cloud

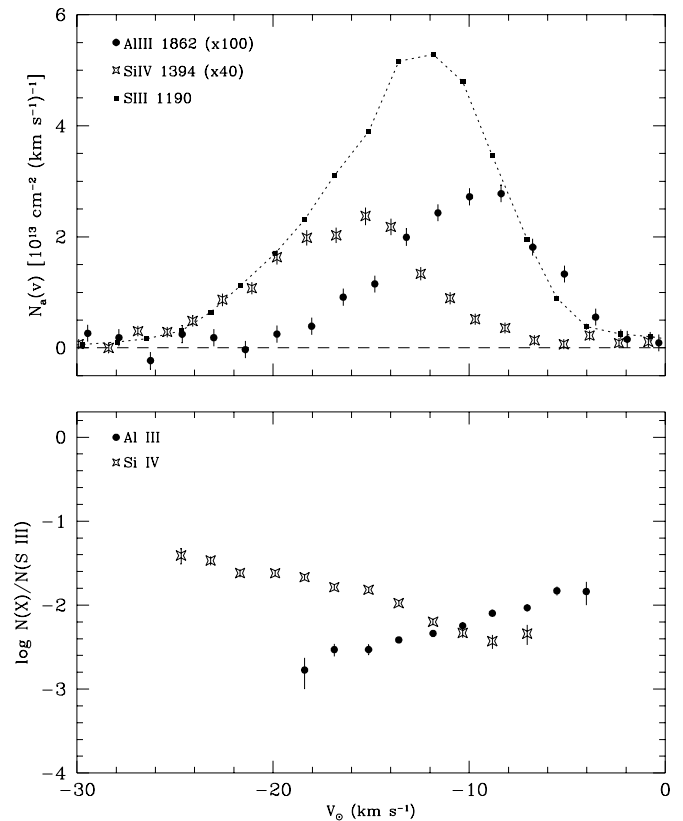


FIG. 3.—*Top panel:* Apparent column density profiles of Al III, S III, and Si IV observed toward ζ Oph at 3.5 km s^{-1} resolution displayed on a heliocentric velocity scale. The profiles of Al III and Si IV have been scaled upward by factors of 100 and 40, respectively. *Bottom panel:* Logarithm of the ratio of Al III and Si IV to S III as a function of velocity.

seen in the Zn II profile (see also Savage, Cardelli, & Sofia 1992).

Figure 3 shows the complexities that arise when looking in detail at a given interstellar sight line. The other sight lines in our sample may be similarly complex, with complications hidden in the absorption profiles. The modeling we present in § 4.1 is highly idealized and does not account for the physics of stellar wind bow shocks, for example. For the ζ Oph sight line we will give results derived from the integrated sight-line values of $N(\text{Al III})$ and $N(\text{S III})$; we will, however, note the results for the case of $\log N(\text{Al III})/N(\text{S III}) \approx -2.0$ along this sight line, which is appropriate for gas associated with the strongest component of Al III along this sight line.

3.2. The High-Latitude Sight Lines to HD 18100 and ρ Leo

The average electron densities toward the higher latitude stars can be estimated using the $^2P_{3/2}$ fine structure level of C II (denoted C II*). SS96 have studied the excitation of C II* toward HD 18100. They find, assuming the excitation is caused by electron collisions, $\langle n_e \rangle = 0.071 \text{ cm}^{-3}$. This treatment assumes that all of the C II* and S II along the line of sight arise in the same gas and is a lower limit to the true electron density in the ionized gas. The value $\langle n_e \rangle$ for ρ Leo given in Table 2 is our own determination assuming electron collisions are populating the upper fine-structure level of C II. We have measured $\log N(\text{C II}^*) = 14.13 \pm 0.02$ and $\log N(\text{S II}) = 15.51 \pm 0.02$ from archival GHRS data for this sight line. The column of C II* was derived from observations using the G160M grating and should be considered

a lower limit given the possible presence of unresolved saturated structure. The average electron density is then determined using equation (7) of SF93, although we adopt $[C/S] \approx [C/H] = -0.4$ from Cardelli et al. (1996). We find $\langle n_e \rangle \geq (0.074 \pm 0.005)(T/6000 \text{ K})^{0.5} \text{ cm}^{-3}$. Thus $\langle n_e \rangle$ toward ρ Leo is similar to that toward the halo stars HD 18100 and HD 93521 as well as the direction toward 3C 273, which also probes halo gas.³ Reynolds (1991a) finds the high-latitude WIM is clumped in regions having electron densities $\langle n_e \rangle \approx 0.08 \text{ cm}^{-3}$, a value quite close to the average densities derived for the high-latitude sight lines discussed here.

For the two distant high-latitude stars HD 18100 and ρ Leo, we find a very good velocity correspondence between low-ionization gas (traced, for example, by Zn II) and ionized gas traced by Al III and S III. Savage & Sembach (1994, 1996b) present GHRs observations of the high and low stages of ionization, respectively, toward HD 18100. The low-ionization lines along this sight line are found at the same velocities as Al III and S III, as well as the high-ionization species such as Si IV and C IV; Savage & Sembach (1994) find the observed profile widths increase with the ionization potential of the species.

Toward ρ Leo we also see that the Al III and Zn II profiles are quite similar, showing two principal absorbing components (blends) centered at velocities $v_\odot \approx -7$ and $+20 \text{ km s}^{-1}$. To show this correspondence more clearly, we plot the apparent column density profiles (Savage & Sembach 1991) of Zn II, S III, and Al III for the sight line toward ρ Leo in Figure 4. Also shown is the profile of the $^2P_{3/2}$ C II fine structure level as observed by the GHRs G160M grating with a resolution of $\sim 17 \text{ km s}^{-1}$ (FWHM). The absolute velocity scale of the C II* observations was determined through the use of a SPYBAL observations as discussed in § 2. The nominal wavelengths were shifted by -0.039 \AA (or -8.7 km s^{-1} at 1335.77 \AA) based upon the analysis of the SPYBAL observations.

The apparent column density profiles of Al III and S III have shapes very similar to the Zn II profile, and the alignment of the Al III and Zn II component structure is excellent. The S III profile is systematically shifted by $\sim -2.2 \text{ km s}^{-1}$ with respect to Zn II. This may be due to uncertainties in the absolute velocity scale; however, Fitzpatrick & Spitzer (1994) have found a similar offset (-2.4 km s^{-1}) in their S III observations toward γ^2 Vel and suggested a possible error in the rest wavelength of the transition. Given the similarities of the two profiles, we have applied a $+2.2 \text{ km s}^{-1}$ shift to the observed S III velocities in producing the profile in Figure 4. The profile for C II*, which is likely tracing thermal electrons that are responsible for exciting C II to the fine structure level (see SF93), also seems to trace the Zn II component structure very well, although the difference in resolution between the two data sets make a direct comparison somewhat uncertain.

The detailed velocity correspondence between tracers of ionized and primarily neutral gas seen toward the two high- z stars in our sample suggests the ionized gas is associ-

³ The cooling rate per neutral H atom for the ρ Leo sight line in the C II $158 \mu\text{m}$ line is therefore also similar to these other halo sight lines, with $l_c \geq (1.4 \pm 0.3) \times 10^{-26} \text{ ergs s}^{-1} (\text{H atom})^{-1}$. The cooling in the $158 \mu\text{m}$ line along the ζ Oph and ζ Per sight lines may be as low as a factor of 5 below this value (Gry, Lequeux, & Boulanger 1992), further illustrating the differences in the ionized gas along the low- and high-latitude sight lines.

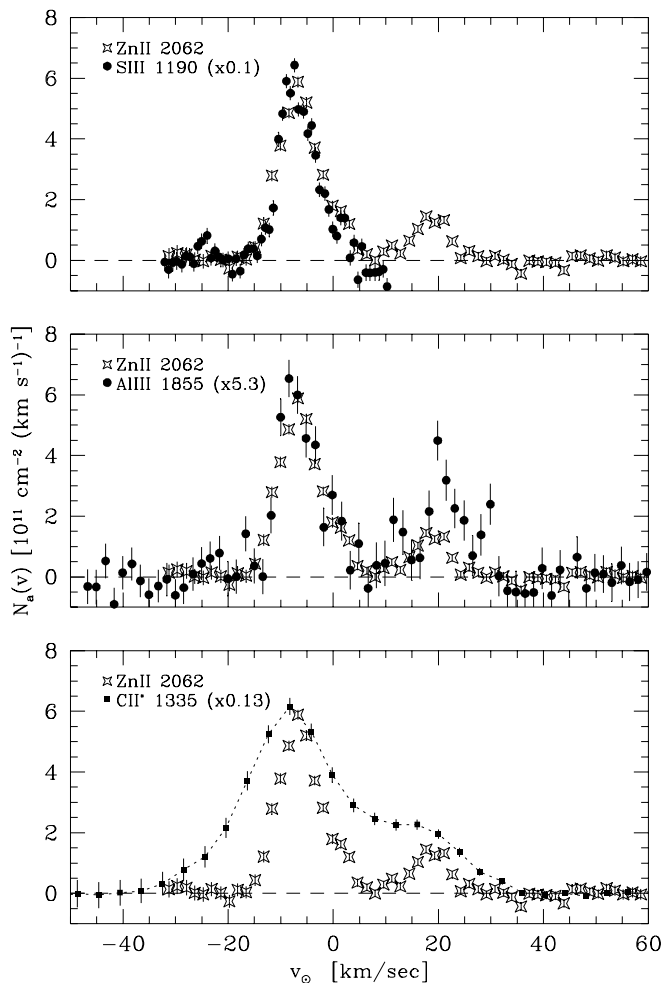


FIG. 4.—Apparent column density profiles of S III, Al III, C II*, and Zn II toward ρ Leo plotted against heliocentric velocity. The C II* observations were obtained with the G160M grating, the other measurements were made with the GHRs echelle gratings. The profiles of the first three ions have been scaled to match that of Zn II. The scale factors are noted in the plots. The S III profile has been shifted by $+2.2 \text{ km s}^{-1}$ (see text). The S III profile is not plotted for $v_\odot > 5 \text{ km s}^{-1}$ because of strong contamination with intermediate negative velocity Si II $\lambda 1190.416$ absorption components.

ated physically with the neutral material. *There is no kinematic evidence that the ionized and neutral phases are spatially separated toward ρ Leo.* The good velocity correspondence between neutral and ionized gas tracers could arise if S III and Al III absorption were tracing ionized edges of neutral clouds (e.g., McKee & Ostriker 1977) or if the clouds seen toward these high-latitude stars were partially ionized with neutral and ionized tracers mixed (e.g., SF93). The kinematic profiles in our data do not allow us to distinguish between these two scenarios, or other more complex arrangements of the two phases. The ionized and neutral media along the HD 18100 sight line seem to show a similarly close relationship, although we will not make as strong a claim in this case given the lower resolution of the data. The ionization produced by decaying neutrinos as proposed by Sciama (1995, 1997) would result in partially ionized gas. However, the decay photons from neutrinos with $E_\nu = 13.7 \pm 0.1 \text{ eV}$ (Sciama 1995) are incapable of ionizing Al^+ and S^+ . Therefore other sources of ionization (e.g., star light, X-ray background photons, or collisional

ionization) are required to produce the Al^{+2} and S^{+2} we observe.

The close association of neutral and ionized tracers was also observed along the sight line to HD 93521 by SF93, a high-latitude star at $z \approx 1500$ pc from the Galactic plane. The component structure along the sight line toward HD 93521 is more complex than that toward ρ Leo, but the correspondence between C II* and tracers of neutral gas (e.g., S II) is very good. SF93 interpreted the data for the HD 93521 sight line to imply the free electrons and neutral gas were cospatial and well mixed. Thus they argue for the existence of a partially ionized phase of the ISM at high- z .

Recent WHAM observations of the Perseus arm have shown the intensity ratio of [O I] $\lambda 6300$ to $\text{H}\alpha$ is in the range 0.01–0.04 (Reynolds et al. 1998a). The weakness of [O I] emission implies the fractional ionization in the WIM of the Galaxy is very high, since the ionization of O and H are strongly coupled through charge-exchange reactions. Reynolds et al. comment that the observed ratio implies that most of the observed emission from the Galactic WIM cannot arise from partially ionized gas along these sight lines, which probe gas at distances from the plane $|z| \lesssim 300$ pc. Similar results have been obtained for the WIM in the edge-on galaxy NGC 891 (Dettmar & Schulz 1992; Rand 1998). The assumption by SF93 of a partially ionized phase of the ISM would seem to be contradicted by these [O I] measurements, although the WHAM observations were taken along a different path through the ISM and probe distances $z \lesssim 300$ pc.

Further high-resolution observations of neutral and ionized gas tracers will help to disentangle the connections between these phases of the ISM. Given the presence of C IV and N V absorption at similar velocities toward HD 18100, it is also possible that these high-latitude sight lines are not tracing gas photoionized by stellar radiation but rather photoionization by cooling hot gas or more complicated interactions between various phases of the ISM, such as conductive interfaces or turbulent mixing layers (see SS96 and references therein). The contribution to the column densities of S III and Al III by hot, collisionally ionized gas could compromise our results and is discussed in § 4.4.

Although the source of ionization of the WIM is not well understood, in § 4.3 we will derive the gas-phase abundances in the ionized gas toward the high-latitude stars ρ Leo and HD 18100 by assuming the clouds to be photoionized by radiation from OB stars.

4. GAS-PHASE ABUNDANCES IN IONIZED GAS

Deriving the gas-phase abundance of Al relative to S from the column densities of Al III and S III requires the application of an ionization correction factor (ICF) to account for the unobserved ionization stages of Al and S (primarily Al^+ and S^+). The logarithmic gas phase abundance normalized to solar, $[\text{Al}/\text{S}]_i$, where the subscript i denotes this value in the ionized gas, is related to the measured column densities of S III and Al III by

$$[\text{Al}/\text{S}]_i \equiv \log(N(\text{Al}^{+2})/N(\text{S}^{+2})) - \log(x(\text{Al}^{+2})/x(\text{S}^{+2})) - \log(\text{Al}/\text{S}_\odot), \quad (5)$$

where $x(\text{Al}^{+2}) \equiv N(\text{Al}^{+2})/N(\text{Al})$ and $x(\text{S}^{+2}) \equiv N(\text{S}^{+2})/N(\text{S})$ are the ionization fractions of Al^{+2} and S^{+2} in the ionized gas. The ratio $(x(\text{Al}^{+2})/x(\text{S}^{+2}))^{-1}$ is the ICF, which we will

write $\text{ICF}(\text{Al}^{+2})$. More generally, in this work $\text{ICF}(X^i) \equiv (x(X^i)/x(\text{S}^{+2}))^{-1}$.

In this section we derive $x(\text{Al}^{+2})/x(\text{S}^{+2})$ for moderate to low-density ionized gas near late-O/early-B stars. We then apply the ICFs to our measurements to derive gas-phase abundances $[\text{Al}/\text{S}]_i$.

4.1. CLOUDY Photoionization Equilibrium Models

We use the photoionization equilibrium code CLOUDY (v90.04; Ferland 1996 and Ferland et al. 1998) to model the ionization and temperature structure of diffuse, low-excitation H II regions. Our models assume spherically symmetric nebulae excited by a single star. We use a volume-filling factor f , which is the fraction of the volume filled with constant hydrogen particle density n_{H} (in cm^{-3}); the rest of the space is assumed to be filled with very tenuous material and in these models is treated as a vacuum. From the radially averaged ionization structure of the nebula, we can derive the ICF appropriate for direct measures of the column densities toward the central ionizing stars.

We use ATLAS line-blanketed, LTE stellar atmosphere models (Kurucz 1991) as input spectra to the CLOUDY models. Our models follow the temperature and ionization structure of the model H II region from 0.3 pc distance from the exciting star to the point where the electron density falls to $< 5\%$ the ambient density n_{H} (i.e., $x(\text{H}^0) = 0.95$). While the models we present here assume solar abundances with no dust opacity, we have found the inclusion of subsolar abundances of the refractory elements and the addition of dust grain opacity does not significantly alter our conclusions. This is because highly refractory elements, i.e., Fe, Ni, Al, Cr, and so on, are not dominant nebular coolants. Further, grain opacity tends to mimic the absorbing characteristics of H; including this opacity therefore removes the same ionizing photons as H (see Mathis 1986b). While the inclusion of photoelectric heating by dust and the absence of minor nebular coolants may have a more pronounced effect on the predicted emission line strengths, these thermal differences cause little or no change in the predicted ionization fractions, and hence the column densities, of the species we are considering. Detailed descriptions of our use of CLOUDY models to gain information regarding the high-ionization species toward μ Col and the contribution of H II region material to the neutral tracers toward this star can be found in Brandt et al. (1999) and Howk et al. (1999), respectively.

We have computed a grid of model H II regions with varying input spectra and ambient densities. Table 5 gives the radially averaged ionization fractions for several UV tracers of photoionized gas in model H II regions. These models used ATLAS model atmospheres with $T_{\text{eff}} = 33,000$ K, $\log L_*/L_\odot = 4.4$, and solar system abundances. This stellar effective temperature and luminosity are appropriate for μ Col or ζ Oph. We have adopted $f = 1.0$ in these models while varying the ambient density of the gas. Many authors define an ionization parameter, which is related to the ratio of hydrogen-ionizing photon density, n_γ , to particle density, n_{H} , in the ionized region. A traditional definition of the ionization parameter (e.g., Mathis 1986b; Shields & Kennicutt 1995) is

$$U \equiv \frac{L}{4\pi R_\zeta^2 n_{\text{H}} c}, \quad (6)$$

TABLE 5
CLOUDY H II REGION MODEL FOR AN O9.5 V STAR^a

$n_{\text{H}}^{\text{b}}(\text{cm}^{-3})$	$\log q^{\text{c}}$	$\log U^{\text{d}}$	$\log x(\text{S}^{+2})^{\text{e}}$	$\log x(X^i)/x(\text{S}^{+2})^{\text{f}}$				
				Al ⁺²	Fe ⁺²	Si ⁺²	Si ⁺³	P ⁺²
0.02	-4.1	-4.3	-0.45	-0.25	0.24	-0.15	-2.03	-0.01
0.05	-3.7	-4.1	-0.40	-0.24	0.21	-0.13	-2.08	-0.01
0.1	-3.4	-4.0	-0.36	-0.23	0.19	-0.12	-2.14	-0.02
0.2	-3.1	-3.9	-0.33	-0.23	0.17	-0.11	-2.22	-0.02
0.5	-2.7	-3.8	-0.28	-0.22	0.14	-0.10	-2.36	-0.02
1.0	-2.4	-3.7	-0.25	-0.21	0.12	-0.09	-2.46	-0.02
1.5	-2.2	-3.6	-0.24	-0.20	0.11	-0.09	-2.55	-0.02
10.0	-1.4	-3.4	-0.18	-0.18	0.08	-0.07	-2.94	-0.02
100.0	-0.4	-3.0	-0.15	-0.20	0.10	-0.06	-3.77	-0.03

^a The ionization fractions reported here are the radially averaged values of nebular models with an input stellar effective temperature $T_{\text{eff}} = 33,000$ K and total luminosity $\log L_{\star}/L_{\odot} = 4.4$. The ionizing photon luminosity in these models is $\approx 4 \times 10^{47}$ photons s^{-1} .

^b Total hydrogen density (neutral plus ionized) used in the model.

^c $q \equiv n_{\text{H}} f^2 L_{50}$, where n_{H} is the ambient hydrogen density, f is the filling factor, and L_{50} is the stellar ionizing flux in units of 10^{50} photons s^{-1} .

^d $U \equiv L/(4\pi R_{\text{S}}^2 n_{\text{H}} c)$, where n_{H} is the ambient hydrogen density and L is the hydrogen ionizing photon luminosity in photons s^{-1} . The Strömgen radius is $R_{\text{S}} = [3L/(4\pi n_{\text{H}}^2 f \alpha_{\text{B}})]^{1/3}$, where α_{B} is the case B recombination coefficient of H. We give values assuming $\alpha_{\text{B}} = 2.59 \times 10^{-13}$ $\text{cm}^3 \text{s}^{-1}$ appropriate for $T_e = 10^4$ K (Osterbrock 1989).

^e $\log x(\text{S}^{+2})x(\text{S}^{+2}) \equiv N(\text{S}^{+2})/N(\text{S}_{\text{Total}})$.

^f These columns give $\log x(X^i)/x(\text{S}^{+2}) \equiv -\log \text{ICF}$ (see § 4).

where L is the hydrogen ionizing photon luminosity in photons s^{-1} and the Strömgen radius is $R_{\text{S}} = [3L/(4\pi n_{\text{H}}^2 f \alpha_{\text{B}})]^{1/3}$, where α_{B} is the case B recombination coefficient of H (Osterbrock 1989), and f is again the volume-filling factor. Using this definition $U \propto n_{\text{H}}^{1/3}$, and we find $3U = \langle n_{\text{H}}/n_{\text{H}} \rangle$, where the average is over volume. In this work we will primarily adopt the equivalent definition given by Domgörgen & Mathis (1994, hereafter DM94). We write the alternate ionization parameter q as

$$q \equiv n_{\text{H}} f^2 L_{50}, \quad (7)$$

where L_{50} is the stellar ionizing luminosity in units of 10^{50} photons s^{-1} . This definition is related to the traditional U by $q = 10^{-50}(36\pi c^3/\alpha_{\text{B}}^2)U^3$, although it removes the dependence on temperature that is hidden in α_{B} (Osterbrock 1989). Bright high-density H II regions are typically described by models with $\log q \gtrsim -1.0$, while DM94 use $-4.0 \lesssim \log q \lesssim -3.0$ in modeling the Galactic WIM. We give the value of $\log q$ for each model in Table 5 for comparison with the models of DM94, Mathis (1986a), and others. We also give the equivalent values of $\log U$. The values U quoted assume $\alpha_{\text{B}} = 2.59 \times 10^{-13}$ $\text{cm}^3 \text{s}^{-1}$ appropriate for $T_e = 10^4$ K (Osterbrock 1989).

In general, the ionization and thermal structure of low-density models is determined by the ionization parameter, the adopted gas-phase abundances, and the shape of the ionizing continuum. Table 5 shows the ionization fraction of S^{+2} is a function of the ionization parameter q ; however, the ratios of the ionization fractions $x(\text{Al}^{+2})/x(\text{S}^{+2})$, $x(\text{Si}^{+2})/x(\text{S}^{+2})$, and $x(\text{P}^{+2})/x(\text{S}^{+2})$ are quite insensitive to changes in q for a given stellar effective temperature. Furthermore, these ratios, which give us the ICF for determining the relative gas-phase abundances of Al, Si, and P to S, are not large. The greatest correction, for Al, is only of order ~ 0.2 dex. The ICF relating $N(\text{Fe III})/N(\text{S III})$ to $[\text{Fe/S}]_i$ is also relatively well-behaved with respect to the ionization parameter, but we shall see that it shows substantial variation with the input stellar effective temperature.

Table 6 gives the ratios of ionization fractions for $\log q = -4.0$ as a function of stellar effective temperature in the range $27,000 \leq T_{\text{eff}} \leq 39,000$. One can see that the relative ionization fractions $x(X^i)/x(\text{S}^{+2})$ are more sensitive to changes in the shape of the underlying continuum than to changes in the ionization parameter q . Even so, the spread of values $x(\text{Al}^{+2})/x(\text{S}^{+2})$, $x(\text{Si}^{+2})/x(\text{S}^{+2})$, and $x(\text{P}^{+2})/x(\text{S}^{+2})$ are still relatively small. Table 6 also gives the average ionization corrections appropriate for relating the ratio of the various ionized species to their gas-phase abundances in the ionized gas. Two values are given: one representing the radially averaged physical properties of the nebula (ICF_{Rad}) and one representing the volume-averaged properties (ICF_{Vol}). The radially averaged values are appropriate for the sight lines that primarily probe absorption through H II regions toward the exciting stars. The volume-averaged ICFs are more appropriate for random interceptions of unrelated H II regions or the WIM. The volume-averaged ICFs tend to weight the outer portions of the model nebulae more strongly, and therefore the volume-averaged values tend to favor lower stages of ionization. This can be seen in the difference between $\log \langle \text{ICF}(\text{Si}^{+3})_{\text{Vol}} \rangle$ and $\log \langle \text{ICF}(\text{Si}^{+3})_{\text{Rad}} \rangle$ in Table 6: the radially averaged ICF suggests a greater fraction of Si is in Si^{+3} than in the volume-averaged case. The ICFs given at the bottom of Table 6 are averages over the seven stellar effective temperatures considered in our models with $\log q = -4.0$ and -2.0 . Also given are the standard deviations about the means. The standard deviations give us a measure of how sensitive our derived ICFs are to uncertainties in the effective temperature of the ionizing radiation source, and we will use these values as estimates of the errors in our derived ICFs.

In Figure 5 we show $\log (x(X^i)/x(\text{S}^{+2}))$ as a function of T_{eff} for the ionized species $X^i = \text{Al}^{+2}$, Fe^{+2} , Si^{+2} , P^{+2} , C^{+2} , and N^{+2} . Also shown in the bottom panel of this figure are the logarithms of $x(\text{S}^{+2})$, $x(\text{Al}^{+2})$, and $x(\text{Fe}^{+2})$. It is clear that the ICFs relating these ions to the gas-phase

TABLE 6
CLOUDY H II REGION MODEL FOR $\log q = -4.0^a$

$T_{\text{eff}}(\text{K})$	$\log x(\text{S}^{+2})$	$\log x(X^i)/x(\text{S}^{+2})$				
		Al^{+2}	Fe^{+2}	Si^{+2}	Si^{+3}	P^{+2}
27,000	-0.71	-0.11	0.55	0.12	-4.93	0.12
29,000	-0.58	-0.16	0.40	-0.01	-3.85	0.05
31,000	-0.49	-0.21	0.30	-0.10	-2.78	0.01
33,000	-0.44	-0.25	0.23	-0.14	-2.04	-0.01
35,000	-0.40	-0.30	0.15	-0.19	-1.58	-0.04
37,000	-0.37	-0.33	0.10	-0.22	-1.43	-0.06
39,000	-0.34	-0.36	0.04	-0.27	-1.30	-0.10
$\log \langle \text{ICF} \rangle_{\text{Rad}}^b$		$+0.24 \pm 0.07$	-0.17 ± 0.19	$+0.10 \pm 0.10$	$+2.6 \pm 1.4^c$	$+0.01 \pm 0.06$
$\log \langle \text{ICF} \rangle_{\text{Vol}}^d$		$+0.37 \pm 0.07$	-0.4 ± 0.3	$+0.38 \pm 0.21$	$+4.3 \pm 1.4^c$	-0.05 ± 0.08

^a The ionization fractions and ratios reported here are the radially averaged values of nebular models with $\log q \equiv \log(n_{\text{H}} f^2 L_{50}) = -4.0$. The alternate definition of the ionization parameter gives $\log U \equiv \log(L/(4\pi R_S^2 n_{\text{H}} c)) = -4.22$ assuming $\alpha_B = 2.59 \times 10^{-13} \text{ cm}^3 \text{ s}^{-1}$ appropriate for $T_e = 10^4 \text{ K}$ (Osterbrock 1989).

^b The mean value of the radially averaged ionization corrections and standard deviation about the mean for each species considered. These numbers are the average and dispersion of the ICFs for all stellar effective temperatures considered for models having $\log q = -4.0$ and -2.0 .

^c The values of $\text{ICF}(\text{Si}^{+3})$ are highly uncertain given the strong dependence upon the stellar effective temperature and ionization parameter.

^d The mean value of the volume-averaged ionization corrections and standard deviation about the mean for each species considered. These numbers are the average and dispersion of the ICFs for all stellar temperatures considered for models having $\log q = -4.0$ and -2.0 .

abundances of these elements (relative to S) in the ionized gas are functions of the assumed stellar effective temperatures. However, for Al III, Si III, and P III, the dependence on T_{eff} is relatively small, having a *total* spread of $\lesssim 0.25$ dex over the range $29,000 \leq T_{\text{eff}} \leq 39,000 \text{ K}$. The bottom panel shows that, even when S^{+2} and Al^{+2} are not

the dominant ionization stages of Al and S, the fractional abundances of the two ions follow each other very well. The 1σ uncertainties quoted for the ratios of ionic column densities using absorption-line spectroscopy are often ~ 0.1 dex (e.g., Savage et al. 1992; SF93; Howk et al. 1999), which is similar to or greater than the standard deviations found for the predicted ICFs given in Table 6 for Al III, Si III, and P III relative to S III.

The ICF for Fe III (also C III and N III) shows a greater dependence on the effective temperature of the underlying stellar atmosphere than those for Al III, Si III, and P III. However, even uncertainties on the order 0.2–0.3 dex for the value of $\text{ICF}(\text{Fe}^{+2})$ can distinguish between depleted and nondepleted abundance ratios for an element that is typically found to be as heavily incorporated into grains as Fe.

A concern when interpreting these results is the accuracy of the atomic data used in deriving these models. In particular, the atomic data for Fe are a concern (e.g., Bautista & Pradhan 1998). The atomic data adopted by CLOUDY are discussed in Ferland (1996) and Ferland et al. (1998). In general, the photoionization cross-sections (using fits to the Opacity Project results by Verner et al. 1996) and radiative recombination rates (see references in Ferland et al. 1998) are relatively secure. The dielectronic recombination coefficients α_{di} for recombinations into the first two ions of Al are also relatively secure (Nussbaumer & Storey 1986). Although $\alpha_{\text{di}}(\text{Al}^{+2})$ and $\alpha_{\text{di}}(\text{Al}^{+3})$ are estimated, Ferland (1996) predicts the ionization balance of $\text{Al}^0 - \text{Al}^{+2}$ is relatively reliable. The low-temperature dielectronic recombination coefficients for the various ionic stages of S, Si, and Fe are not well constrained (Ferland 1996; Ferland et al. 1998).

CLOUDY estimates the unknown low-temperature dielectronic recombination coefficients of the first four ionization stages of elements in the third and fourth rows of the periodic table by adopting a mean of the rate coefficients for the first four ionization stages of C, N, and O (Ali et al.

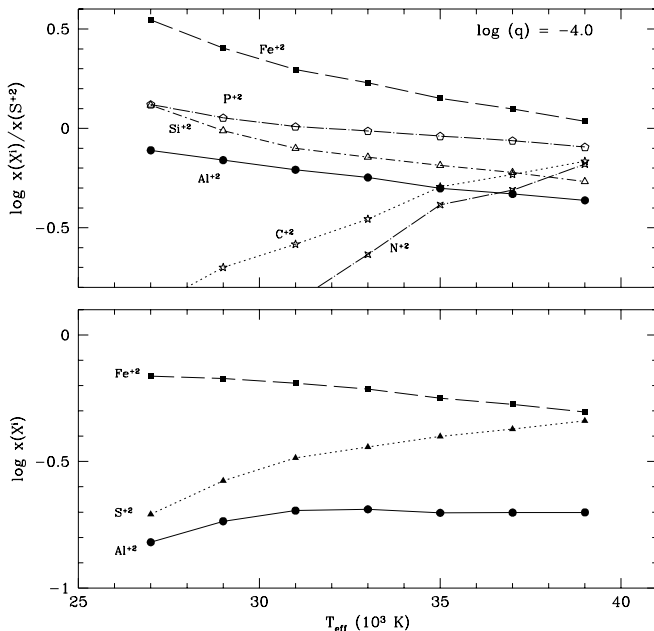


FIG. 5.—Values of $\log x(X^i)/x(\text{S}^{+2}) = -\log \text{ICF}(X^i)$ for several tracers of ionized gas as a function of the effective temperature, T_{eff} , of the ionizing star. The fractional ionization $x(X^i) \equiv N(X^i)/N(X)$ is derived using column densities integrated from the star to the edge of the model H II region. These data are for models characterized by the ionization parameter $\log q = -4.0$. Also shown in the bottom panel is the behavior of the ionization fractions $x(\text{S}^{+2})$, $x(\text{Fe}^{+2})$, and $x(\text{Al}^{+2})$ as a function of the assumed stellar effective temperature.

1991).⁴ We have disabled CLOUDY's approximation of α_{di} for these elements to test its effects on the observed ratios. The ICFs derived for Al^{+2} , Si^{+2} , and P^{+2} differ in models with and without the assumptions regarding dielectronic recombination by less than the standard deviations given in Table 6. For Fe III, the models with $\alpha_{\text{di}}(\text{Fe}^i) = 0.0$ give values close to that given in Table 6. However, the density dependence of $x(\text{Fe}^{+2})/x(\text{S}^{+2})$ is greatly increased. The values of $\text{ICF}(\text{Fe}^{+2})$ are less certain than the ICFs for the other species considered here, given their strong dependence on the shape of the ionizing spectrum. The same can be said for $\text{ICF}(\text{Si}^{+3})$.

The adopted error of $\sigma = 0.2\text{--}0.3$ dex for $\text{ICF}(\text{Fe}^{+2})$ likely encompasses enough of parameter space to make our error estimates not unreasonable. We will make estimates for $[\text{Fe}/\text{S}]_i$ where the data for Fe III are available, but it is important to recognize the strong dependence of the ionization correction on T_{eff} and the possibly inappropriate atomic parameters for Fe.

4.2. $[\text{Al}/\text{S}]_i$ and $[\text{Fe}/\text{S}]_i$ in H II Regions

In this section we derive $[\text{Al}/\text{S}]_i$ and $[\text{Fe}/\text{S}]_i$ for the sight lines probing H II regions in the Galactic disk. The results of § 4.1 give ICFs that are directly applicable to H II regions about the stars ζ Oph, ξ Per, β^1 Sco, and μ Col. The distances to these stars are small enough that it may be reasonable to assume their H II regions dominate the column density of ions considered here. For ζ Oph this comparison is complicated by the velocity structure, which suggests there are a number of processes at work along this sight line. A comparison of the integrated column densities of Al III and S III toward this star will not necessarily provide us a good measure of the gas phase abundance $[\text{Al}/\text{S}]_i$. As discussed in § 3.1, the sight line toward μ Col may be probing H II region or WIM gas, or a mixture of both. We will assume here that the ionized gas along this sight line is probing an H II region.

Table 7 presents the observed ratios of the integrated column densities of Al III and Fe III (where available) to S III for our program stars. Also given in this table are the derived logarithmic abundances $[\text{Al}/\text{S}]_i$ and $[\text{Fe}/\text{S}]_i$. The abundances $[\text{Al}/\text{S}]_i$ and $[\text{Fe}/\text{S}]_i$ for the sight lines to μ Col, ξ Per, β^1 Sco, and ζ Oph were derived using the ICFs appropriate for the stellar effective temperatures of these

⁴ The adopted coefficients for the first four ionization stages of third and fourth row elements are $\alpha_{\text{di}}(\text{X}^0) = 3 \times 10^{-13}$, $\alpha_{\text{di}}(\text{X}^+) = 3 \times 10^{-12}$, $\alpha_{\text{di}}(\text{X}^{+2}) = 1.5 \times 10^{-11}$, and $\alpha_{\text{di}}(\text{X}^{+3}) = 2.5 \times 10^{-11} \text{ cm}^3 \text{ s}^{-1}$. These are adopted from Nussbaumer & Storey (1983).

stars, with the error estimates as discussed in § 4.1. We are assuming in this approach that the measured material is mostly photoionized H II region gas. Given the velocity structure discussed in § 3.1.1, $[\text{Al}/\text{S}]_i$ in the ζ Oph H II region may be as high as -1.0 . The values $[\text{Al}/\text{S}]_i$ and $[\text{Fe}/\text{S}]_i$ presented in Table 7 for these disk sight lines suggest grains are present in the H II regions surrounding all of these stars.

Federman et al. (1993) present a GHRs measurement of P III $\lambda 1334.813$ along the sight line to ζ Oph. They find $\log N(\text{P III}) = 12.94 \pm 0.04$. From the results presented in Table 6, we see $\log \text{ICF}(\text{P}^{+2}) = +0.01 \pm 0.06$. We thus find $[\text{P}/\text{S}]_i = -0.11 \pm 0.07$ for the ionized gas toward ζ Oph. This value assumes the integrated sight-line column densities of P and S are tracing the same regions, which may be incorrect given the velocity structure toward this star (§ 3.1.1). The element P is thought to be very lightly depleted. In their study of the neutral gas abundances along the ζ Oph sight line, Savage et al. (1992) find $[\text{P}/\text{H}] = -0.23$ for the warm neutral cloud centered at $v_{\odot} = -27 \text{ km s}^{-1}$ (their component A). For the sight line toward μ Col, Howk et al. (1998) derive $[\text{P}/\text{S}] = -0.03 \pm 0.03$ in the low-velocity absorbing complex centered at $v_{\odot} = +23 \text{ km s}^{-1}$, which shows abundance patterns similar to component A toward ζ Oph. The $[\text{P}/\text{S}]_i$ derived here for the ζ Oph sight line is consistent with previous $[\text{P}/\text{S}]$ measurements for neutral material: P is lightly depleted, if at all.

4.3. $[\text{Al}/\text{S}]_i$ in the WIM

In this subsection we consider the gas-phase abundances $[\text{Al}/\text{S}]_i$ in the halo WIM. The interpretation of the $N(\text{Al III})/N(\text{S III})$ measurements along the sight lines to ρ Leo and HD 18100 is subject to uncertainties regarding the ionization of the WIM and contamination from collisionally ionized gas (see § 4.4). The long path-lengths through the WIM and the likelihood that any H II regions around these stars are in very low-density environments imply that a large fraction of the observed Al III and S III along these sight lines arises in the WIM of our Galaxy. ρ Leo should lie above $\sim 60\%$ of the WIM of the Galaxy, while HD 18100 should lie above almost all of the high- z layer of ionized material (Reynolds 1989; Savage et al. 1990). Although the ionization source of the diffuse ionized material is not well known, the power requirements suggest ionization by OB stars may be a viable mechanism (Reynolds 1984; DM94). Here we estimate $[\text{Al}/\text{S}]_i$ toward ρ Leo and HD 18100 for the case where the WIM of the Galaxy is photoionized by OB stars.

We will follow DM94 and model the WIM of the Milky Way using low-density H II region photoionization models.

TABLE 7
COLUMN DENSITY RATIOS AND LOGARITHMIC GAS-PHASE ABUNDANCES

Star	$\log N(\text{Al III}) / N(\text{S III})$	$\log N(\text{Fe III}) / N(\text{S III})$	$[\text{Al}/\text{S}]_i$	$[\text{Fe}/\text{S}]_i$
ζ Per	-1.97 ± 0.03	...	-0.87 ± 0.08	...
μ Col	-1.82 ± 0.05	-0.40 ± 0.11	-0.78 ± 0.08	-0.87 ± 0.21
ζ Oph ^a	-2.23 ± 0.03	-1.05 ± 0.10	-1.19 ± 0.08	-1.52 ± 0.21
β^1 Sco	-1.92 ± 0.09	-0.88 ± 0.12	-1.00 ± 0.11	-1.59 ± 0.21
ρ Leo	-1.66 ± 0.06	...	-0.50 ± 0.10^b	...
HD 18100	-1.59 ± 0.07	...	-0.43 ± 0.10^b	...

^a The values given here for ζ Oph are the for the integrated sight line.

^b The values given here for $[\text{Al}/\text{S}]_i$ toward ρ Leo and HD 18100 assume the shape of the ionizing spectrum of the diffuse ionized gas is not very different than that of a star with $27,000 \lesssim T_{\text{eff}} \lesssim 39,000 \text{ K}$.

The ratio $x(\text{Al}^{+2})/x(\text{S}^{+2})$ derived for our H II region models is relatively insensitive to the ionization parameter and is not heavily dependent on the shape of the input ionizing spectrum; we therefore believe it is appropriate to apply the results derived in § 4.1 to the WIM of the Galaxy. Our observations of ionized gas toward ρ Leo and HD 18100 probe the WIM and thus are not a simple radial integration through an H II region. A volume-averaged set of ICFs are more appropriate for application to the WIM than the radially averaged values used in the previous subsection (DM94). Volume-averaged ICFs from the models treated in § 4.1 are given in the last row of Table 6. We see that there are significant differences in the ICFs derived for most of the ions studied here when adopting volume versus radially averaged values.

We do not know well the shape of the ionizing spectrum appropriate for the WIM. We will continue by adopting the mean of the volume-averaged values $\text{ICF}(\text{Al}^{+2})$ for our models. These values are given in Table 6 as ICF_{vol} . The values $[\text{Al}/\text{S}]_i$ given for HD 18100 and ρ Leo in Table 7 are therefore derived assuming $\log(x(\text{Al}^{+2})/x(\text{S}^{+2})) = -0.37 \pm 0.07$ or $\log \text{ICF}(\text{Al}^{+2}) = +0.37$ in the WIM. For the sight line toward μ Col, the value $[\text{Al}/\text{S}]_i$ given in Table 7 was derived assuming $\log \text{ICF}(\text{Al}^{+2}) = +0.25 \pm 0.07$ in an H II region about this star; if this sight line instead probes the WIM along this direction, the gas-phase abundance could be $[\text{Al}/\text{S}]_i = -0.66 \pm 0.08$.

We can estimate values for $\log x(\text{S}^{+2})$ along our two high-latitude sight lines. Assuming $N_e = 7 \times 10^{19}/\sin |b| \text{ cm}^{-2}$ (Reynolds 1991b) and accounting for the 40% of this value expected to reside beyond ρ Leo, the predicted electron column densities along the high-latitude sight lines are $\log N_e = 19.7$ and 19.9 for ρ Leo and HD 18100, respectively. Assuming $N_e \approx N(\text{H}^+)$ and the solar abundance of S/H (Anders & Grevesse 1989), for ρ Leo and HD 18100 we find $\log x(\text{S}^{+2}) \sim -1.3$ and -0.9 , respectively. Compared with our *volume-averaged* results for models having $\log q = -4.0$, this implies the characteristic “effective temperature” for the ionizing radiation field of $28,000 \lesssim T_{\text{eff}} \lesssim 33,000$ K is appropriate for these sight lines.⁵ This result is consistent with the limits derived from observations of diffuse He I recombination radiation (Reynolds & Tufté 1995).

The Al III and S III data presented here, when compared with our model results, are inconsistent with a solar relative abundance of Al to S in the WIM. We have assumed that the intrinsic or cosmic abundance (gas plus dust) of Al to S is given by the solar system values. Even in the presence of mildly subsolar metallicities, $[\text{X}/\text{H}] \gtrsim -1.0$, the abundance of Al relative to S is expected to be quite close to the solar abundance. Although Al is an odd-Z element, it is primarily produced in the C- and Ne-burning stages of massive stars. Thus S and Al are both deposited into the ISM by Type II supernovae.

In their study of elemental abundances in solar neighborhood low-mass stars, Edvardsson et al. (1993) derive abundances for Al as well as several α -elements. The behavior of $[\text{Al}/\text{Fe}]$ versus $[\text{Fe}/\text{H}]$ in their data set mimics that of the

⁵ It is important to note that we are using the *volume-averaged* ICFs here rather than the radially averaged values given in Table 6. For models having $\log q = -4.0$, we find $\log x(\text{S}^{+2}) = -1.38, -1.16, -0.99, -0.84, -0.77$, and -0.53 for $T_{\text{eff}} = (27, 29, 31, 33, 35, 37, \text{ and } 39) \times 10^3$ K, respectively, in the volume-averaged model results.

TABLE 8
MEASUREMENTS OF Si IV COLUMN DENSITIES

Star	$\log N(\text{Si IV})$	$\log [N(\text{Si IV})/N(\text{S III})]$	Reference
ζ Per	12.89 ± 0.03	-1.93	1
μ Col	12.17 ± 0.05	-1.65	2
ζ Oph	12.79 ± 0.02	-1.97^a	3
β^1 Sco	12.02 ± 0.03	-1.96	1
ρ Leo	$< 11.6^b$	$< -2.1^b$	1
HD 18100.....	13.10 ± 0.04	-1.19	4

^a The value $\log [N(\text{Si IV})/N(\text{S III})]$ given for the ζ Oph sight line is the value integrated over all velocities. Figure 3 shows that this ratio is a strong function of velocity. Near $v_{\odot} \approx -15 \text{ km s}^{-1}$, corresponding to the peak of the Si IV absorption, a value of -1.6 to -1.8 is more appropriate; while, at the peak of the Al III absorption near $v_{\odot} \approx -8 \text{ km s}^{-1}$, $\log [N(\text{Si IV})/N(\text{S III})] \approx -2.4$ is more appropriate.

^b This 2σ upper limit to $\log N(\text{Si IV})$ for the ρ Leo sight line only applies to the velocity range $v_{\odot} = -19$ to $+2 \text{ km s}^{-1}$ (the range over which the S III measurements are made). There is detectable Si IV absorption at more positive velocities. The integrated sight-line column density is $\log N(\text{Si IV}) = 12.24^{+0.07}_{-0.09}$.

REFERENCES.—(1) This work; (2) Brandt et al 1999; (3) Sembach et al 1994; (4) Sembach & Savage 1994.

α -elements.⁶ For their sample of 189 stars, all having $[\text{Fe}/\text{H}] \gtrsim -1.0$, the average value of $[\text{Al}/\alpha]$ is $+0.02 \pm 0.07$, where α in this context represents an average over the elements Mg, Si, Ca, and Ti. The yield of Al relative to the α -elements does depend upon the initial stellar abundances, but this effect is negligible for the range of metallicities of the Edvardsson et al. sample (and for our halo clouds). We do not expect the intrinsic ratio of Al/S, as long as the metallicity of the gas is $\gtrsim 0.1$ solar, to be significantly different than the solar-system value adopted here. Therefore the values of $[\text{Al}/\text{S}]_i < 0.0$ presented here for the WIM are not due to nucleosynthetic effects and imply the existence of dust in this phase of the ISM.

4.4. Collisionally Ionized Gas and its Effects on $[\text{Al}/\text{S}]_i$

If hot, collisionally ionized gas is present along the sight lines studied here, its imprint on the ionization balance of the gas could cause us to misinterpret the column density ratios given in Table 7. The collisional ionization equilibrium models of Sutherland & Dopita (1993), for example, suggest that for gas with temperatures $T \sim 50,000$ K ($\log T = 4.7$), $\log(x(\text{Al}^{+2})/x(\text{S}^{+2})) = -0.93$. Therefore, if one of our sight lines were dominated by gas in collisional ionization equilibrium at this temperature, with $[\text{Al}/\text{S}]_i = 0$, i.e., no depletion, we would erroneously derive $[\text{Al}/\text{S}]_i \approx -0.5$ by assuming the value of $\langle \text{ICF} \rangle_{\text{vol}}$ given in Table 6. While the assumption of collisional ionization equilibrium is not likely to be valid, this calculation suggests the presence of gas with $T \gtrsim 30,000$ K along our sight lines could compromise our conclusions. In this section we will give evidence suggesting, for most of our sight lines, it is unlikely our results are strongly affected by contamination from collisionally ionized gas.

As a first step for approaching the problem, we have collected column density measurements of Si IV and the ratio of Si IV and S III column densities for all of our sight lines in Table 8. Several of the Si IV column densities given in Table 8 are taken from literature measurements using the

⁶ The element S is not included in their data set, although see Wheeler, Sneden, & Truran (1989) and references therein.

GHRS (with references given in the table); others were derived from archival GHRS spectra using the techniques described in § 2. With an ionization potential of 33.5 eV, the ion Si IV is potentially a tracer of collisionally ionized gas with T in the range $(0.3\text{--}1) \times 10^5$ K, although Si IV can also be produced in warm gas via photoionization by hot stars.

In the following discussion we consider the observational constraints regarding collisional ionization for each sight line.

ζ Oph: The absorption toward ζ Oph, as discussed in § 3.1.1 and shown in Figure 3, shows evidence for changes in the ionization structure as a function of heliocentric velocity. The gas at $v_{\odot} \lesssim -15$ km s $^{-1}$ is characterized by large amounts of Si IV absorption and relatively low amounts of Al III. Higher velocity gas along this sight line, $-13 \lesssim v_{\odot} \lesssim -5$ km s $^{-1}$, shows relatively little Si IV and higher ratios of Al III to S III. The peak of the Si IV profile may trace gas that is collisionally ionized. Our CLOUDY models (e.g., Table 5) cannot explain the large value of the ratio $\log(N(\text{Si IV})/N(\text{S III})) \approx -1.8$ observed near $v_{\odot} \approx -20$ km s $^{-1}$. However, Sembach et al. (1994) note that the Si IV line width implies gas with $T < 5 \times 10^4$ K. This temperature limit and the absence of associated C IV absorption lead Sembach et al. to suggest the Si IV absorption is due to photoionized gas in an expanding H II region. The gas between $v_{\odot} = -8$ and -13 km s $^{-1}$ is also likely photoionized gas in the H II region about ζ Oph. This gas shows values of $\log(N(\text{Si IV})/N(\text{S III})) \lesssim -2.0$, which can be generally explained by photoionization models. The profile width of the Al III absorption measured by Sembach et al. (1994) implies gas with $T < 3 \times 10^4$ K. Morton (1975) also finds absorption from N II, N II*, and N II** at $v_{\odot} = -8$ km s $^{-1}$, suggesting the presence of (photo)ionized gas and a significant density of electrons at these velocities. Our earlier suggestion that a value of $\log(N(\text{Al III})/N(\text{S III})) \approx -2.0$ is most appropriate for the photoionized H II region gas toward ζ Oph is based upon the observed ratio at velocities corresponding to the peak of the Al III (and N II) absorption. Reynolds (1988) has observed H α emission centered at $v_{\odot} = -13 \pm 1$ km s $^{-1}$ along this sight line, which is quite near the peak of the S III absorption. The temperature implied by an analysis of the breadth of the [S II] and H α emission profiles is $T = 6700 \pm 700$ K (Reynolds 1988). Thus if we associate the H α and [S II] emission with the absorption seen in S III, Al III, and N II, the temperatures are too low to produce significant amounts of these ions through collisional ionization.

ξ Per: The sight line toward ξ Per shows a complex of H α -emitting regions at several different velocities. Reynolds (1988) finds ionized regions excited by this star at velocities $v_{\odot} = +3, +7, +12,$ and $+14$ km s $^{-1}$. Figure 8 shows the $N_a(v)$ profiles of S III, Al III, and Si IV toward ξ Per and the ratios of the latter two ions to S III, as Figure 3 did for ζ Oph. The vertical dashed lines in this figure represent the velocities at which Reynolds (1988) detects H α emission, though shifted by -2.2 km s $^{-1}$. The peaks in the $N_a(v)$ profile for S III give a good match to the components detected in emission by Reynolds. In his analysis, Reynolds (1988) used the emission from [S II] and H α to separate the thermal and nonthermal components of the observed velocity widths. He found that the emitting regions excited by ξ Per had temperatures between $T \approx 5,000$ and $11,000$ K, consistent with expectations for photoionized gas. We associate the emitting regions studied by Reynolds with the

material seen in S III and Al III absorption in our GHRS spectra. At the implied temperatures, the contribution to the S III and Al III column densities from collisionally ionized gas should be negligible. The ICFs derived using photoionization models should therefore be appropriate for this material.

β^1 Sco: The derived $\log N(\text{Si IV})/N(\text{S III})$ toward β^1 Sco is quite similar to the measured values along the ζ Oph and ξ Per sight lines. Unfortunately, we have virtually no information on the velocity structure of the S III absorption profile given the low resolution of the G160M data. The logarithmic ratio of $\log N(\text{Si IV})/N(\text{Al III})$ is in the range $-0.2\text{--}0.0$ over the velocity range of Al III absorption. The profile-weighted average velocities (Sembach & Savage 1992) for Al III and Si IV are $\langle v_{\odot} \rangle = -13.9 \pm 0.6$ and -11.4 ± 0.5 km s $^{-1}$, respectively. It is tempting to use the similarities between the ζ Oph and β^1 Sco sight lines to argue that collisionally ionized gas is not confusing our analysis of this sight line. The neutral gas absorption profiles toward these stars are very similar (e.g., the Zn II profiles of Figure 1), and the two stars lie at approximately the same distance from the Sun and from the Galactic midplane. However, the differences in spectral type would suggest that in the case of purely photoionized gas and equal gas densities, the ratio $N(\text{Si IV})/N(\text{S III})$ should be smaller for β^1 Sco, i.e., for the star with lower T_{eff} . Also, we have seen (§ 3.1.1) that there are some peculiarities along the ζ Oph sight line, possibly including the presence of collisionally ionized gas at velocities $v_{\odot} \lesssim -15$ km s $^{-1}$. We cannot rule out contributions from collisionally ionized gas to the S III and Al III absorption toward β^1 Sco.

μ Col: For the sight line toward μ Col, measurements with the WHAM Fabry-Perot spectrometer (Reynolds et al. 1998b) show the H α emission is at velocities consistent with the S III absorption profile. The WHAM measurements, with a 1° beam, are well fitted by a Gaussian with $\langle v_{\odot} \rangle = 22.9 \pm 0.5$ km s $^{-1}$ and $b = 17.0 \pm 1.5$ km s $^{-1}$ (M. Haffner 1998, private communication). The breadth of the profile suggests that the gas traced by this emission has $T \lesssim 18,000$ K; in collisional ionization equilibrium models of gas at this temperature, S III and Al III represent less than 1% of the total S and Al abundances (Sutherland & Dopita 1993). The profile-weighted average velocity (Sembach & Savage 1992) of the S III is $\langle v_{\odot} \rangle = 23.2 \pm 0.3$ km s $^{-1}$, with the Al III $\lambda\lambda 1855$ and 1862 lines having $\langle v_{\odot} \rangle = 21.4 \pm 1.0$ and 23.9 ± 0.9 km s $^{-1}$, respectively. Because of the similarity of the velocities, we associate the H α -emitting gas with the S III and Al III absorption. The temperature limits set by the WHAM spectra of this sight line suggest that the contribution of hot, collisionally ionized gas to the S III and Al III column densities is small.

ρ Leo: The archival GHRS spectra of Si IV toward ρ Leo show no evidence for absorption in the velocity range covered by the S III absorption studied here (i.e., $-19 \leq v_{\odot} \leq +2$ km s $^{-1}$). The 2σ upper limit to $N(\text{Si IV})$ given in Table 8 implies $\log(N(\text{Si IV})/N(\text{S III})) \leq -2.1$ in this velocity range, assuming $b_{\text{Si IV}} \approx 10$ km s $^{-1}$. Although there is Si IV absorption overlapping the higher velocity Al III absorption, it appears to be significantly broader than the Al III absorption. We believe that the lack of detectable Si IV absorption at the velocities of the stronger absorbing complex seen in Al III (and S III), with limits that place the ratio $N(\text{Si IV})/N(\text{S III})$ at levels well below those detected along our H II region sight lines, suggests collisionally

ionized gas is not an important contributor to the column densities of Al III and S III toward ρ Leo.

HD 18100: The sight line toward the star HD 18100 has been studied by Sembach & Savage (1994), and their values of $N(\text{Si IV})$ are given in Table 8. As mentioned in § 3.2, the velocities of S III and Al III along this sight line are quite similar to those of the low ions (e.g., Zn II and Mn II), as well as those of the highly ionized species Si IV and C IV. Indeed, Figure 4 of Sembach & Savage (1994) shows that the profiles of Al III, Si IV, and C IV are quite similar as viewed with the resolution of the GHRM G160M grating. Although the breadth of the profiles increases with ionization potential along this sequence, the increase seems mostly to occur toward negative velocities. It is possible that the highly ionized species discussed by Sembach & Savage have more complex velocity structures that would reveal themselves at higher resolution (the 1.4 km s^{-1} resolution Ca II profile presented by SS96 and Ryans et al. 1996 shows evidence for many closely spaced absorbing components along this sight line). However, we have no evidence with which to rule out the possibility that the observed columns of S III and Al III are produced in collisionally ionized gas. The Si IV and C IV absorption profiles, which are at the same velocities as the lower ionization species, suggest that such contamination may indeed be a real problem for this sight line. That the ratio of $N(\text{Si IV})/N(\text{S III})$ along this sight line is the highest in our sample also suggests collisionally ionized gas may be playing a role in determining the ionization balance in the gas we are studying. Thus our application of the ICFs derived from photoionization for this sight line may be inappropriate.

In summary, with the exception of the sight line to HD 18100 and possibly β^1 Sco, it appears that collisional ionization does not likely explain the origin of the Al III and S III. In the case of HD 18100, the velocity overlap of the absorption due to low, moderate, and highly ionized species, as well as the large column density of Si IV relative to S III, raises the possibility that much of the observed Al III and S III along this sight line could arise in collisionally ionized gas.

5. DISCUSSION

The Al III and S III column densities, when combined with the results of our photoionization modeling, suggest that Al-bearing dust is indeed present in the ionized gas along the sight lines considered here. For H II region gas, this result is not surprising. The existence of dust in H II regions has been implied by several independent lines of reasoning (see Osterbrock 1989, chap. 7; Mathis 1986b; Peimbert & Goldsmith 1972), although little can be discerned about the composition of the grains or the degree to which dust grains are processed in the ionized ISM using these methods.

Our measurements of $[\text{Al}/\text{S}]_i$ for the nearby sight lines that probe the H II regions surrounding the stars ζ Oph, ξ Per, β^1 Sco, and μ Col give us a measure of the incorporation of Al into dust grains in these nebulae. Assuming $[\text{Al}/\text{S}]_i = [\text{Al}/\text{H}]_i$, the dust-phase abundances of Al in the ionized material along these sight lines, in units of atoms per million hydrogen, are $10^6(\text{Al}/\text{H})_d \equiv 10^6(\text{Al}/\text{H})_\odot - 10^6(\text{Al}/\text{H})_i = 2.8 \pm 0.6$, 2.6 ± 0.5 , 2.7 ± 0.8 , and 2.5 ± 0.5 for ζ Oph, ξ Per, β^1 Sco, and μ Col, respectively. These values are an order of magnitude less than the dust-phase abundance of Fe, Si, or Mg in the warm neutral ISM (Savage & Sembach 1999b; Howk et al. 1998). The dust-

phase abundances of Al presented here are similar to the values derived for Ni in the WNM, which has a similar solar system abundance (Savage & Sembach 1996b; Howk et al. 1999).

Unfortunately, little is known about the gas-phase abundance of Al in the WNM of the Galaxy because of the great strength of the only available Al II transition at 1670 Å. Barker et al. (1984) have performed a curve-of-growth analysis of interstellar Al II absorption in the WNM using data from the *Copernicus* observatory. However, for many of their sight lines the absorption due to Al is far up the flat portion of the curve of growth, making the uncertainties in the determination of the Al column densities quite large. In deriving the column density of Al II, Barker et al. employ an empirical curve of growth derived from Si II. However, since Al and Si are expected to have different gas-phase abundances from component to component due to changing depletion effects, it is likely that Si II and Al II have somewhat different curves of growth. Jenkins (1983), with several important caveats summarized at the beginning of his paper, has compared the equivalent widths of Al II $\lambda 1670$ with the similarly strong Si II transition at 1304 Å. While the nature of his comparison tends to heavily weight low-column density, intermediate-velocity features, Jenkins finds no evidence for changing $[\text{Al}/\text{Si}]$ with z -height of the probe star with the implied value $[\text{Al}/\text{Si}] \approx -0.2$. This is near the upper range found by Barker et al. (1984) but is roughly consistent with their values. Again, there are many uncertainties with Jenkins' approach, among them that the Al II and Si II transitions are likely both on the flat part of the curve of growth, which may hide significant changes in the relative abundances.

For comparison with our results, we look to those sight lines with the least saturated lines in the Barker et al. (1984) survey. For these sight lines, Barker and coworkers consistently find $[\text{Al}/\text{H}] \approx -1.1$ to -1.0 . This selection is strongly biased toward low-density sight lines. If we take $[\text{Al}/\text{S}]_i \approx -1.0$ as representative of the H II region sight lines in our sample, this suggests the refractory grain material is not heavily affected by the conditions in low-density H II regions. However, the validity of this comparison is somewhat suspect given the uncertainties and biases in the Barker et al. results.

Our estimates of $[\text{Fe}/\text{S}]_i$ in three of the sight lines considered here (see Table 7) yield values roughly consistent with those for $[\text{Fe}/\text{H}]_i$ in the Orion nebula from a variety of authors (Osterbrock, Tran, & Veilleux 1992; Peimbert, Torres-Peimbert, & Dufour 1993; Baldwin et al. 1996; Rodríguez 1996; Rubin et al. 1997) and suggest Fe is incorporated into grains in these ionized regions. The relative values $[\text{Al}/\text{S}]_i$ versus $[\text{Fe}/\text{S}]_i$ suggest that the fraction of Al incorporated into grains is consistent with that of Fe or a bit less. For the sight lines toward ζ Oph and μ Col, we can directly compare the gas-phase abundances of Fe derived for the neutral and ionized sight lines. In each case, the velocity of the ionized gas is closest to the components that show the lowest value of $[\text{Fe}/\text{H}]$, which are $[\text{Fe}/\text{H}] = -2.4$ for ζ Oph (Savage et al. 1992) and $[\text{Fe}/\text{H}] \approx [\text{Fe}/\text{S}] = -1.3$ for μ Col (Sofia, Savage, & Cardelli 1993; Howk et al. 1999). Using the values of $[\text{Fe}/\text{S}]_i$ given in Table 7, we find that $\sim 3\%$ and $\sim 9\%$ of the dust-phase Fe in the neutral gas has been returned to the gas-phase in the ionized gas (with a factor of 2 uncertainty). Our measurements of significantly subsolar Al and Fe abundances in H II regions suggest the

processing of grains in low-excitation H II regions is not much different than the destruction that occurs in the WNM of the Galaxy.

The implications of dust within H II regions have been discussed by several authors (e.g., Shields & Kennicutt 1995; Henry 1993; McGaugh 1991; Aannestad 1989; Mathis 1986b). The most important effects are caused by the incorporation of possibly important coolants into the solid phase (Shields & Kennicutt 1995), the change in the thermal balance due to photoelectron emission (heating) and far-infrared (FIR) thermal dust emission (cooling), and the competition of the dust opacity with H and He for ionizing photons (Mathis 1986b). McGaugh (1991) has shown that the existence of dust can significantly alter the Balmer line strengths expected from an H II region. This effect comes about because the dust is able to absorb a significant number of photons that would otherwise go toward ionizing H (Mathis 1986b). As a consequence, McGaugh suggests calculations of the star formation rates using only Balmer line intensities may underestimate the number of ionizing stars present. Also, the true volume of a dusty H II region will be smaller than the dust-free Strömgen volume. For low-density H II regions like those studied here, however, Mathis (1986b) has shown that the effects of dust absorption may not provide a significant optical depth to ionizing photons. Mathis also points out that although dust is an additional source of opacity, the opacity due to dust does not affect the ionization balance of most species in H II regions given its similarity to the H opacity. Shields & Kennicutt (1995) discuss the important effects of dust on emission line strengths from metal-rich ($Z > Z_{\odot}$) H II regions, particularly those found near the centers of galaxies.

Sembach & Savage (1996) have shown that, in general, the gas-phase abundances of elements increases as one moves from the disk to the halo of our galaxy. This suggests an increasing degree of (incomplete) grain destruction with increasing height above the plane of the Galaxy. In Figure 6 we show the gas-phase abundances $[Al/S]_i$ as a function of

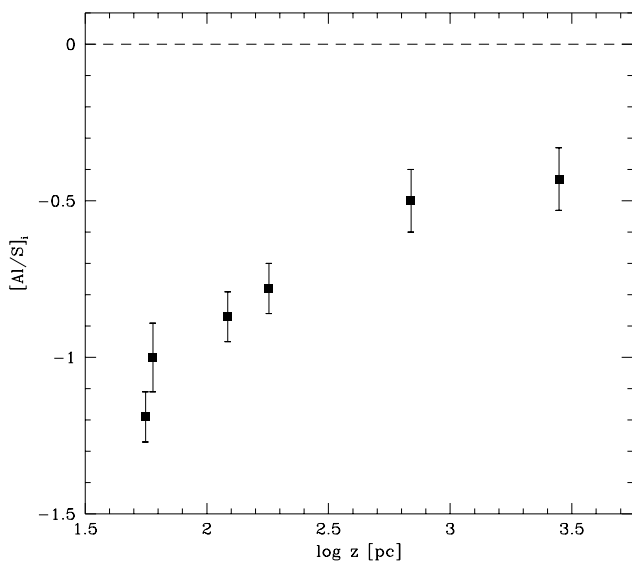


FIG. 6.—Behavior of $[Al/S]_i = \log(Al/S)_i - \log(Al/S)_{\odot}$ as a function of z -height of the probe star. Since S is not depleted onto grains, $[Al/S]_i \approx [Al/H]_i$ gives a measure of the fraction of Al incorporated into dust grains in the ionized gas.

z -distance of the observed stars. Since S is generally not depleted, $[Al/S]_i$ should closely follow $[Al/H]_i$. There is a general trend of increasing gas-phase abundance of Al in the ionized gas with increasing height above the plane of the Galaxy. This is qualitatively consistent with the behavior observed by Sembach & Savage for the WNM.

It is also known that the gas-phase abundances of elements increase with decreasing $\langle n_H \rangle \equiv N(H\text{ I})/d$ in the warm neutral ISM (Jenkins 1987; Savage & Bohlin 1979). Both the ionized and neutral gas densities are thought to decrease exponentially with z -height (Dickey & Lockman 1990; Reynolds 1989), suggesting that the behavior seen in Figure 6 may be tracing the density-dependence of the gas. In Figure 7 we plot the values $[Al/S]_i$ versus the electron density (*top*) and the average line of sight neutral density (*bottom*), as given in Table 2. Given the many definitions of the electron densities (average vs. rms and so on), we have used different symbols to represent the determinations of rms and average electron densities (see § 3).

Figure 7 shows a striking relationship between the average densities and the gas-phase abundances of $[Al/S]_i$ along the sight lines considered here. We find that the gas-phase abundance $[Al/S]_i$ increases with decreasing electron densities. The observed relationship between $[Al/S]_i$ and n_e is similar to the observed dependence of WNM abundances on average sight-line neutral hydrogen ($H\text{ I} + H_2$) density (Edgar & Savage 1989; Jenkins 1987; Savage & Bohlin 1979). The slope of $[Al/S]_i$ versus $\log n_e$ is -0.37 , similar to the value -0.38 derived for $[Fe/H]$ versus $\log \langle n_H \rangle$ by Jenkins (1987).

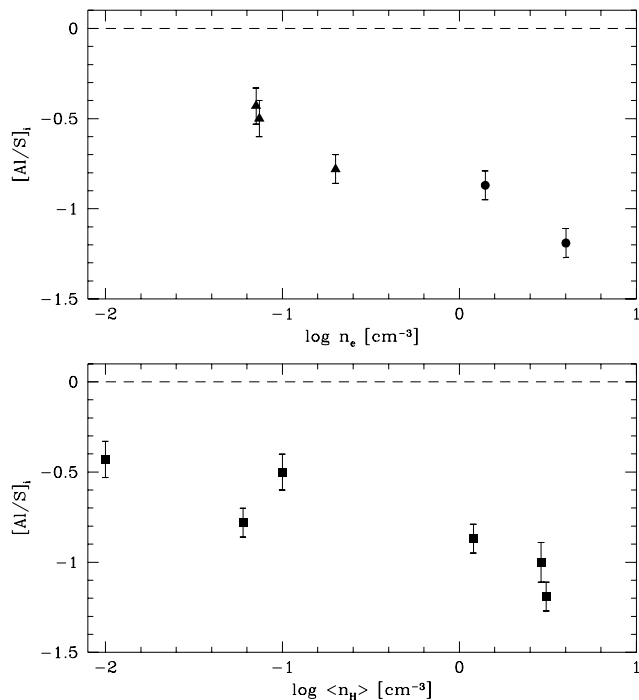


FIG. 7.—Behavior of $[Al/S]_i \equiv \log(Al/S)_i - \log(Al/S)_{\odot}$ as a function of average density. Since S is not depleted onto grains, $[Al/S]_i \approx [Al/H]_i$ gives a measure of the fraction of Al incorporated into dust grains in the ionized gas. The bottom panel shows $[Al/S]_i$ versus the average sight-line neutral density $\langle n_H \rangle \equiv [N(H\text{ I}) + 2N(H_2)]/d$. The top panel shows $[Al/S]_i$ versus the electron density n_e . The filled circles in the top panel represent determinations of rms electron densities $\langle n_e \rangle^{1/2}$, and the triangles are for determinations of average electron densities $\langle n_e \rangle$.

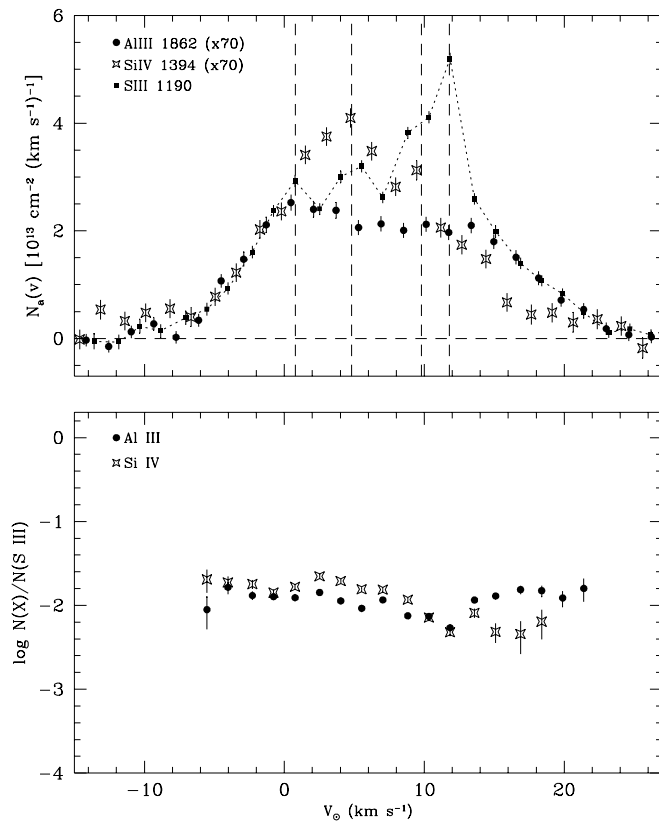


FIG. 8.—*Top panel:* Apparent column density profiles of Al III, S III, and Si IV observed toward ξ Per at 3.5 km s^{-1} resolution displayed on a heliocentric velocity scale. The profiles of Al III and Si IV have been scaled upward by a factor of 70. *Bottom panel:* Logarithm of the ratio of Al III and Si IV to S III as a function of velocity. The vertical dotted lines of the top panel represent the velocities of H α emission detected by Reynolds (1988), though shifted by -2.2 km s^{-1} .

Although we are measuring the gas-phase abundance $[\text{Al}/\text{S}]_i$, i.e., the abundance of Al to S in the *ionized* gas, the bottom panel of Figure 7 shows a significant correlation between $[\text{Al}/\text{S}]_i$ and $\log \langle n_{\text{H}} \rangle$, the average line-of-sight *neutral* density. Savage et al. (1990) have also noted a correlation of $\log N(\text{Al III})/N(\text{H I})$ with decreasing $\log \langle n_{\text{H}} \rangle$. These authors point out that this trend may be due to the changing ionization fraction of Al^{+2} with density, to changing values $[\text{Al}/\text{H}]_i$ with density, or perhaps to both. Figure 7 shows that at least part of the trend observed by Savage et al. is due to the changes in the gas-phase abundance of Al with average neutral density. The trend observed by these authors, which is nicely matched by our data, and that seen in Figure 7 suggest that $\langle n_{\text{H}} \rangle$ is a good indicator of the conditions in the ionized gas. The slope of $[\text{Al}/\text{S}]_i \approx [\text{Al}/\text{H}]_i$ versus $\log \langle n_{\text{H}} \rangle$ in our data is less steep than the slope of $\log N(\text{Al III})/N(\text{H I})$ versus $\log \langle n_{\text{H}} \rangle$ in the Savage et al. data set, suggesting that a combination of changing gas-phase abundances and ionization fraction is causing the trend observed by Savage et al. and that perhaps the behavior seen in Figure 7 is more widespread than our six sight lines.

In general, Figure 7 implies that the ionized and neutral densities along a sight line follow the same trends, i.e., low $\langle n_{\text{H}} \rangle$ also implies low values of n_e . This relationship may simply be a manifestation of the known decrease in both ionized and neutral gas densities as a function of height above the Galactic plane. This is also the expected behavior

if neutral clouds with ionized edges are providing most of the observed absorption (cf. Reynolds et al. 1998a). Spitzer (1985) and Jenkins, Savage, & Spitzer (1986) have interpreted the dependence of elemental gas-phase abundances on the average sight-line density $\langle n_{\text{H}} \rangle$ in the neutral ISM as a dependence on the relative contribution of two neutral media: clouds (cold and warm) and an intercloud medium. In this picture the warm intercloud medium has greater gas-phase abundances than the denser clouds. With an appropriate mix of each medium, the integrated gas-phase abundance for a given line of sight can be reproduced. Perhaps a variation on this scenario is also appropriate for the ionized medium of our Galaxy. The relative mix of clouds may be similar between the neutral and ionized phases depending on the poorly known relationship between these phases.

As discussed in § 4.3, if the WIM of the Galaxy is photoionized by starlight from OB stars (DM94; Reynolds 1984), our measurements of Al III and S III absorption toward HD 18100 and ρ Leo imply the existence of dust in this important phase of the ISM. The values $[\text{Al}/\text{S}]_i$ for ρ Leo and HD 18100 are significantly higher than those for the other four stars (see Figs. 6 and 7), suggesting that the grain population in the high-latitude WIM has undergone a greater degree of processing (e.g., by shocks) than have the grains in the low- z H II regions. For the halo WIM we find a dust phase abundance of $10^6(\text{Al}/\text{H})_d \approx 1.9\text{--}2.1$. It would appear that $\sim 20\%$ – 30% of the Al has been liberated from the solid phase in the high- z WIM compared with the results derived above for the disk H II regions.

Very little is known about dust in the WIM of the Milky Way (or other galaxies) from previous studies. Although in principle one might be able to separate the thermal dust emission in the WIM from that of the H I and H₂ gas, this has proven difficult. Boulanger et al. (1996) have studied the correlation of the FIR flux with the column density of neutral hydrogen $N(\text{H I})$ at high Galactic latitudes. They find that the correlation between the $\lambda 21 \text{ cm}$ H I emission and the FIR emission detected by the *Cosmic Background Explorer* mission is quite good. They are not, however, able to rule out a dust abundance in the WIM similar to that observed in the neutral component.

The existence of dust is important for maintaining the temperature of the WIM (Reynolds & Cox 1992; Dettmar & Schulz 1992). Reynolds & Cox (1992) show that the heating of the WIM may be in large part provided by photoelectron emission from grains. This requires the amount of grain heating per H atom to be similar to that found in the WNM. The presence of grains in the WIM has important ramifications for the diagnostic emission lines used to study this gas. Reynolds & Cox point out that the total heating per H nucleus s^{-1} in the low-density WIM may be twice that of a typical, higher density H II region. This has profound effects on the forbidden lines that provide the cooling for the gas. The increased cooling required over H II region gas increases the ratios of $[\text{S II}]$, $[\text{N II}]$, and $[\text{O III}]$ to H α over H II regions. Reynolds & Cox suggest this extra heating may in part be responsible for the enhanced forbidden line strengths observed from the WIM of our Galaxy and others (Reynolds 1985; Rand 1997).

Our data suggest that the destruction of the dust grains in the high- z WIM has not been extreme. The value $\sim 20\%$ – 30% given above for the amount of Al liberated from the solid- to gas-phase when going from disk H II regions to the

halo WIM is consistent with differential measurements of warm neutral cloud abundances between the disk and the halo. For a small sample of halo and warm disk clouds, Howk et al. (1999) find roughly 20%–30% of the dust-phase Fe and Si on average have been returned to the gas-phase between the disk and halo clouds. Therefore, the processing of grains in the halo WIM does not appear to be significantly greater than that experienced by clouds associated with the halo WNM.

This discussion does not suggest that grain destruction mechanisms have not played an important role in the evolution of the gas being considered. The $\sim 20\%$ – 30% of dust-phase Al we see returned to the gas-phase in the halo WIM may be material that was initially bound in a refractory coating or mantle surrounding the grains. Savage & Sembach (1996b; see their Table 7) have tabulated the dust-phase abundances of a number of elements. The derived dust-phase abundances for the WNM of the Galactic disk give the composition of the grain cores and mantles, and the observed abundances of the halo material gives information on the composition of the resilient grain cores that have probably been stripped of their mantles (Sembach & Savage 1996). Savage & Sembach (1996b) argue that the Fe returned to the gas-phase in halo material comes predominantly from the mantles thought to surround the resilient cores that survive the trip into the halo. They find the dust-phase abundance of Fe in grain cores to be $10^6(\text{Fe}/\text{H})_d = 25$, and for the mantles they find $10^6(\text{Fe}/\text{H})_d = 7$. Thus $\sim 22\%$ of the Fe incorporated into grains in the Milky Way disk resides in a mantle that is relatively easily stripped. The liberated Al seen in the WIM at high z may also come from the mantles of grains, leaving the resilient grain cores to account for the remaining 70%–80% of the Al missing from the gas phase.

In considering the multiphase structure of neutral clouds in the Galactic halo, Wolfire et al. (1995b; see also Wolfire et al. 1995a) show that the stability of multiphase neutral clouds is affected by the intrinsic abundances in the gas and by the dust content of the clouds. Thus the presence of dust in ionized halo clouds will have important implications for the physical structure of the resulting neutral clouds if the ionized gas recombines. Indeed, in the case where the dusty multiphase clouds envisioned by Wolfire et al. (1995b) are situated above the disk of the galaxy, where they are bathed in ionizing radiation from the disk (assuming photons are able to leak out of the disk), they will be surrounded by ionized skins. If no processes beyond photoionization are responsible for producing the ionized edges of such clouds, the differences in the dust content of the neutral and ionized phases should be minimal. This may explain why the gas-phase abundances in the ionized gas toward ρ Leo and HD 18100, where the neutral and ionized phases of the ISM seem to coexist (at least in velocity space), are so similar to the derived refractory element gas-phase abundances in warm neutral halo clouds (Sembach & Savage 1996).

6. SUMMARY

This work represents one of the first absorption-line studies of the WIM of the Galaxy. The observations imply the existence of Al- and Fe-bearing dust grains in the ionized gas of the Galactic disk and halo.

A summary of the work presented here and our major conclusions is as follows:

1. We present archival GHRS intermediate- and high-resolution absorption-line observations of the moderately ionized species Al III and S III in the ionized ISM toward six stars. The sight lines toward ζ Oph, ξ Per, β^1 Sco, and μ Col probe primarily H II region gas in the Galactic disk. The extended high-latitude sight lines toward HD 18100 and ρ Leo probe the WIM of the Galaxy at high z . Results for Fe III from the literature are presented for μ Col, β^1 Sco, and ζ Oph.

2. We show, with the possible exceptions of the sight lines to β^1 Sco and HD 18100, that collisional ionization does not likely explain the origin of the observed amounts of Al III and S III.

3. We have computed a grid of photoionization equilibrium models for low-density regions excited by late-O/early-B stars using the CLOUDY code (Ferland et al. 1998). We show, using our photoionization models, that the ionization corrections for determining $[\text{Al}/\text{S}]_i$, $[\text{P}/\text{S}]_i$, and $[\text{Si}/\text{S}]_i$ using the species Al III, P III, Si III, and S III are relatively insensitive to the ionization parameter and the effective temperature of the ionizing spectrum. Deriving $[\text{Fe}/\text{S}]_i$ from the ratio $N(\text{Fe III})/N(\text{S III})$ requires a greater knowledge of the stellar effective temperature.

4. We derive the logarithmic gas-phase abundances $[\text{Al}/\text{S}]_i \approx [\text{Al}/\text{H}]_i$ in the ionized material toward the six stars in our sample using the results of our photoionization modeling. All of these stars have $[\text{Al}/\text{S}]_i$ ranging from -1.2 to -0.4 . Since S is normally not incorporated into dust, these abundance results indicate the incorporation of Al into dust grains in the ionized material along these six sight lines, although for the most distant stars we cannot rule out the confusing effects of collisional ionization. For three stars we find $[\text{Fe}/\text{S}]_i$ ranges from -1.6 to -0.9 .

5. The gas-phase abundances $[\text{Al}/\text{S}]_i$ and $[\text{Fe}/\text{S}]_i$ derived here for the disk sight lines probing H II region material show that a significant degree of Al incorporation into grains is still present in the vicinity of stars; i.e., neither the UV radiation fields from the stars nor any shocks associated with the stellar winds from these stars are sufficient to completely disrupt the refractory grains. The abundances we derive here are similar to the gas-phase Fe abundances $[\text{Fe}/\text{H}]_i$ derived for the Orion nebula using emission lines (e.g., Osterbrock et al. 1992; Baldwin et al. 1996).

6. If the WIM of the Galaxy is ionized by the light from OB stars (Reynolds 1984), the observed Al III and S III column densities toward HD 18100 and ρ Leo imply the existence of Al-bearing dust in the WIM. To our knowledge this is the first evidence for dust in the Galactic diffuse ionized gas, although the effects of collisional ionization cannot be ruled out, particularly for the sight line toward HD 18100.

7. The gas-phase abundances $[\text{Al}/\text{S}]_i$ in the ionized material increases with height z above the Galactic plane. Furthermore, the values $[\text{Al}/\text{S}]_i$ increase with decreasing average or rms electron densities and with decreasing average sight-line neutral hydrogen density. This behavior is similar to that of the gas-phase refractory abundances in the WNM of the galaxy (Jenkins 1987; Savage & Bohlin 1979). This general trend implies a greater return of elements to the gas phase in more diffuse environments.

8. The observed values of $[\text{Al}/\text{S}]_i$ are similar to the abundances of other refractory elements seen in the WNM of the disk and halo. Furthermore, the variation of $[\text{Al}/\text{S}]_i$ with

density (electron or neutral) is also similar to the values observed for refractory elements in the WNM (especially Fe or Mn). Our analysis implies that the processing of dust grains in the ionized gas may not be much different than that in the low-density WNM.

9. We discuss the velocity structure of the WIM along the two high-latitude sight lines in our sample. These directions show a very close relationship between the tracers of neutral material and ionized gas, similar to the correspondence observed by SF93. The data show no kinematic evidence for a separation of the ionized and neutral material. This is consistent with a partially ionized medium in which the neutrals and ions are well mixed (e.g., SF93), the neutral clouds are surrounded by ionized envelopes (e.g., McKee & Ostriker 1977), or other more complex scenarios.

We have benefited from conversations with R. Reynolds, B. Benjamin, and J. Mathis in preparing this manuscript. We also thank E. Jenkins for a careful reading of our work

and for suggestions that improved the final result. We thank E. Fitzpatrick for sharing his component-fitting software with us, and M. Haffner, R. Reynolds, and the WHAM group for sharing their results in advance of publication. We feel G. Ferland and his coworkers at the University of Kentucky have done a great service for the astronomical community in making available their photoionization code CLOUDY. This work has only proceeded because of our confidence in the implementation of the physics included in CLOUDY.⁷ The archival GHRIS data used here were acquired from the GHRIS Instrument Definition Team archive.⁸ This research has made use of the SIMBAD database, operated at CDS, Strasbourg, France. J. C. H. recognizes support from a NASA Graduate Student Researcher Fellowship under grant NGT-5-50121.

⁷ The CLOUDY code and documentation, e.g., Ferland (1996), can be accessed at <http://www.pa.uky.edu/~gary/cloudy/>.

⁸ The archive can be accessed at <http://hrssun.gsfc.nasa.gov/>.

REFERENCES

- Aannestad, P. A. 1989, *ApJ*, 338, 162
 Ali, B., Blum, R. D., Bumgardner, T. E., Cranmer, S. R., Ferland, G. J., Haefner, R. I., & Tiede, G. P. 1991, *PASP*, 103, 1182
 Anders, E., & Grevesse, N. 1989, *Geochim. Cosmochim. Acta*, 53, 197
 Baldwin, J. A., et al. 1996, *ApJ*, 468, L115
 Barker, E. S., Lugger, P. M., Weiler, E. J., & York, D. G. 1984, *ApJ*, 280, 600
 Bautista, M. A. & Pradhan, A. K. 1998, *ApJ*, 492, 650
 Bohlin, R. C., Savage, B. D., & Drake, J. F. 1978, *ApJ*, 224, 132
 Boulanger, F., Abergel, A., Bernard, J.-P., Burton, W. B., Désert, F.-X., Hartmann, D., Lagache, G., & Puget, J.-L. 1996, *A&A*, 312, 256
 Brandt, et al. 1999, *AJ*, 117, 400
 Cardelli, J. A., & Ebbets, D. C. 1994, in *HST Calibration Workshop: Calibrating Hubble Space Telescope*, ed. J. C. Blades & A. J. Osmier (Baltimore: STScI), 322
 Cardelli, J. A., Ebbets, D. C., & Savage, B. D. 1993, *ApJ*, 413, 401
 Cardelli, J. A., Meyer, D. M., Jura, M., & Savage, B. D. 1996, *ApJ*, 467, 334
 Code, A. D., Bless, R. C., Davis, J., & Brown, R. H. 1976, *ApJ*, 203, 417
 Dettmar, R.-J., & Schulz, H. 1992, *A&A*, 254, L25
 Dickey, J. M., & Lockman, F. J. 1990, *ARA&A*, 28, 215
 Diplas, A., & Savage, B. D. 1994, *ApJS*, 93, 211
 Domgörgen, H. & Mathis, J. S. 1994, *ApJ*, 428, 647 (DM94)
 Duncan, D. K. 1992, *GHRIS Handbook*, Version 3.0 (Baltimore: STScI)
 Edgar, R. J. & Savage, B. D. 1989, *ApJ*, 340, 762
 Edwardsson, B., Andersen, J., Gustafsson, B., Lambert, D. L., Nissen, P. E., & Tomkin, J. 1993, *A&A*, 275, 101
 Federman, S. R., Sheffer, Y., Lambert, D. L., & Gilliland, R. L. 1993, *ApJ*, 413, L51
 Ferland, G. J. 1996, *Hazy: A Brief Introduction to CLOUDY 90*, Univ. Kentucky Dept. Phys. Astron. Int. Rep.
 Ferland, G. J., Korista, K. T., Verner, D. A., Ferguson, J. W., Kingdon, J. B., & Verner, E. M. 1998, *PASP*, 110, 761
 Fitzpatrick, E. L., & Spitzer, L. 1994, *ApJ*, 427, 258
 ———. 1997, *ApJ*, 475, 623
 Grevesse, N., & Noels, A. 1993, in *Origin of the Elements*, ed. N. Prantzos, E. Vangioni-Flam, & M. Casseé (Cambridge: Cambridge Univ. Press), 15
 Gry, C., Lequeux, J., & Boulanger, F. 1992, *A&A*, 266, 457
 Heap, S. R., et al. 1995, *PASP*, 107, 871
 Henry, R. B. C. 1993, *MNRAS*, 261, 306
 Holmgren, D., Hadrava, P., Harmanec, P., Koubsky, P., & Kubat, J. 1997, *A&A*, 322, 565
 Howarth, I. D., & Prinja, R. K. 1989, *ApJS*, 69, 527
 Howk, J. C., Savage, B. D., & Fabian, D. 1999, *ApJ*, submitted
 Jenkins, E. B. 1983, in *Kinematics, Dynamics, and Structure of the Milky Way*, ed. W. L. H. Shuter (Dordrecht: Reidel), 21
 ———. 1987, in *Interstellar Processes*, ed. D. J. Hollenbach & H. A. Thronson, Jr. (Dordrecht: Reidel), 533
 Jenkins, E. B., Savage, B. D., & Spitzer, L. 1986, *ApJ*, 301, 355
 Keenan, F. P., Brown, P. J. F., & Lennon, D. J. 1986, *A&A*, 155, 333
 Keenan, F. P., & Dufton, P. L. 1983, *MNRAS*, 205, 435
 Kulkarni, S. R., & Heiles, C. 1988, in *Galactic and Extragalactic Radio Astronomy*, ed. K. I. Kellerman, & G. L. Verschuur (New York: Springer), 95
 Kurucz, R. L. 1991, in *Proceedings of the Workshop on Precision Photometry: Astrophysics of the Galaxy*, ed. A. C. Davis Philip, A. R. Upgren, & K. A. James (Schenectady: Davis), 27
 Mathis, J. S. 1986a, *ApJ*, 301, 423
 ———. 1986b, *PASP*, 98, 995
 McGaugh, S. S. 1991, *ApJ*, 380, 140
 McKee, C. F. & Ostriker, J. P. 1977, *ApJ*, 218, 148
 Morton, D. C. 1975, *ApJ*, 197, 85
 ———. 1991, *ApJS*, 77, 119
 Nussbaumer, H., & Storey, P. J. 1983, *A&A*, 126, 75
 ———. 1986, *A&AS*, 64, 545
 Osterbrock, D. E. 1989, *Astrophysics of Gaseous Nebulae and Active Galactic Nuclei* (Mill Valley: University Science Books)
 Osterbrock, D. E., Tran, H. D., & Veilleux, S. 1992, *ApJ*, 389
 Peimbert, M., & Goldsmith, D. W. 1972, *A&A*, 19, 398
 Peimbert, M., Torres-Peimbert, S., & Dufour, R. J. 1993, *ApJ*, 418, 760
 Perryman, M. A. C., & the *Hipparcos* Science Team. 1997, *The Hipparcos and Tycho Catalogues*, (ESA SP-1200; Noordwijk: ESA)
 Rand, R. J. 1997, *ApJ*, 474, 129
 ———. 1998, *ApJ*, 501, 137
 Reynolds, R. J. 1984, *ApJ*, 282, 191
 ———. 1985, *ApJ*, 294, 256
 ———. 1988, *ApJ*, 333, 341
 ———. 1989, *ApJ*, 339, L29
 ———. 1991a, *ApJ*, 372, L17
 ———. 1991b, in *IAU Symp. 144, The Interstellar Disk-Halo Connection in Galaxies*, ed. H. Bloemen (Dordrecht: Kluwer), 67
 Reynolds, R. J., & Cox, D. P. 1992, 400, L33
 Reynolds, R. J., Hausen, N. R., Tufté, S. L., & Haffner, L. M. 1998a, *ApJ*, 494, L99
 Reynolds, R. J., & Ogden, P. M. 1982, *AJ*, 87, 306
 Reynolds, R. J., & Tufté, S. L. 1995, *ApJ*, 439, L17
 Reynolds, R. J., Tufté, S. L., Haffner, L. M., Jaehnig, K., & Percival, J. W. 1998b, *PASA*, 15, 14
 Robinson, R. D., et al. 1998, *PASP*, 110, 68
 Rodríguez, M. 1996, *A&A*, 313, L5
 Rubin, R. H., et al. 1997, *ApJ*, 474, L131
 Ryans, R. S. I., Sembach, K. R., & Keenan, F. P. 1996, *A&A*, 314, 609
 Savage, B. D., & Bohlin, R. C. 1979, *ApJ*, 229, 136
 Savage, B. D., Cardelli, J. A., & Sofia, U. J. 1992, *ApJ*, 401, 706
 Savage, B. D., Edgar, R. J., & Diplas, A. 1990, *ApJ*, 361, 107
 Savage, B. D., & Sembach, K. R. 1991, *ApJ*, 379, 245
 ———. 1994, *ApJ*, 434, 145
 ———. 1996a, *ApJ*, 470, 893
 ———. 1996b, *ARA&A*, 34, 279
 Sciama, D. W. 1995, *ApJ*, 448, 667
 ———. 1997, *ApJ*, 488, 234
 Sembach, K. R., & Savage, B. D. 1992, *ApJS*, 83, 147

- Sembach, K. R., & Savage, B. D. 1994, ApJ, 434, 145
———. 1996, ApJ, 457, 211
- Sembach, K. R., Savage, B. D., & Jenkins, E. B. 1994, ApJ, 421, 585
- Shields, J. C., & Kennicutt, R. C. 1995, ApJ, 454, 807
- Shull, J. M., & York, D. G. 1977, ApJ, 211, 803
- Soderblom, D. R., Sherbert, L. E., & Hulbert, S. J. 1993, GHRS Instrument Science Report 52 (Baltimore: STScI)
———. 1994, GHRS Instrument Science Report 53 (Baltimore: STScI)
- Sofia, U. J., & Jenkins, E. B. 1998, ApJ, 499, 951
- Sofia, U. J., Savage, B. D., & Cardelli, J. A. 1993, ApJ, 413, 251
- Sokolov, N. A. 1995, A&AS, 110, 553
- Spitzer, L. 1985, ApJ, 290, L21
- Spitzer, L., & Fitzpatrick, E. L. 1993, ApJ, 409, 299 (SF93)
———. 1995, ApJ, 445, 196
- Sutherland, R. S., & Dopita, M. A. 1993, ApJS, 88, 253
- Taylor, J. H., & Cordes, J. M. 1993, ApJ, 411, 674
- Vacca, W. D., Garmany, C. D., & Shull, J. M. 1996, ApJ, 460, 914
- Verner, D. A., Ferland, G., Korista, K., & Yakovlev, D. G. 1996, ApJ, 465, 487
- Wheeler, J. C., Sneden, C., & Truran, J. W. 1989, ARA&A, 27, 279
- Wolfire, M. G., Hollenbach, D., McKee, C. F., Tielens, A. G. G. M., & Bakes, E. L. O. 1995a, ApJ, 443, 152
- Wolfire, M. G., McKee, C. F., Hollenbach, D., & Tielens, A. G. G. M. 1995b, ApJ, 453, 673